Thesis

Theoretical Simulation of
Scanning Tunneling Microscopy/Spectroscopy
— Beyond LCAO Approximation

LCAO 近似を越えた

走査トンネル顕微鏡・走査トンネル分光の

理論的シミュレーション

Hiroyuki Kageshima

影島博之

Department of Physics,

Faculty of Science,

University of Tokyo

December 1990

Thesis

Theoretical Simulation of

Scanning Tunneling Microscopy/Spectroscopy

— Beyond LCAO Approximation

LCAO 近似を越えた

走査トンネル顕微鏡・走査トンネル分光の

理論的シミュレーション

Hiroyuki Kageshima

影島博之

Department of Physics,

Faculty of Science,

University of Tokyo

December 1990

Thesis

Theoretical Simulation of

Scanning Tunneling Microscopy/Spectroscopy

— Beyond LCAO Approximation

Hiroyuki Kageshima

Department of Physics,
Faculty of Science,
University of Tokyo

December 1990

Acknowledgments

Contents

Chapter 1

Introduction

§1. Scope of the Thesis

The most characteristic feature of the surface of materials comes from the fact that
only the surface can interact directly with the outside system. Recently technology of
microscopical processing of materials has been developed rapidly. This trend empha-
sized the crucial importance of understanding microscopic features of the surfaces.
When we meet a new surface, first we must determine the structure of the surface,
since fresh surfaces of materials have many reconstructing structures, and since their
properties are governed by the structure in atomic level. But there were no per-
fect methods to observe directly the surface in atomic scale, and it obstructed the
development of surface science and technology.

The scanning tunneling microscopy (STM) was developed by Binnig and Rohrer
[1] in such a circumstance. This method is based on a simple principle, though very
high technique is required. In STM, the tunneling current between the tip and the
sample surface is measured, scanning the tip position with keeping the tunneling
current constant. Then the contour of the tip reflects the surface corrugation.

Binnig and Rohrer observed the atomistic STM image of graphite surface [3–7],
and revealed the feature of the electronic states of graphite. The observation of Si(111)
(7×7) surface opened the way discovering the DAS model [8–13]. After that, many
surface superstructures have been analyzed, and plenty of new information has been
reported; it includes microscopic structures of defects and steps on the surface [1,
14–22], structures of organic or biological molecules adsorbed on the surface [23–25,
26–28].

In the development of STM, scanning tunneling spectroscopy (STS) was proposed
[29]. In STS, the tunneling conductance between the tip and the surface is measured
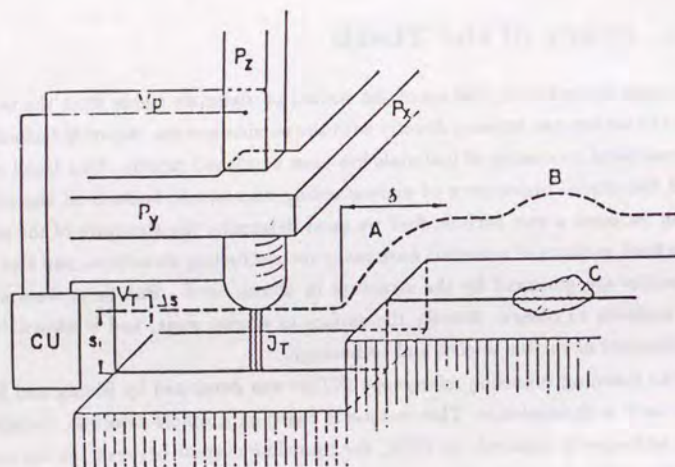
Figure 1.1: Principle of operation of STM (after Binnig *et al.* [1])

varying the tip bias. The differential conductance curve reflects the local density of states (LDOS) at the specific point of the surface. This technique is useful to characterize the local electronic structure of the surface providing extremely rich information of solid surfaces [30].

The most valuable feature of STM is its real space imaging, and that of the STS is its locality. Recently these methods have been developed toward many directions; for example, the atomic force microscopy (AFM) [31] succeeded to observe surfaces of insulating materials in atomic scale by the forces between the tip and the surface. STM is also used in the atomic scale processing of the surface [32]. The Coulomb blockade [33] and negative differential conductance (NDR) [34] reported in STS measurement would lead to atomic scale devices. STM/STS have attracted much attention in many fields.

Today, STM is generally used for observing the surface corrugation. But it would be possible to use STM in conjunction with STS so as to discuss the defect structure or the identification of the observed atom. These discussions, however, would be only possible under the help of theoretical works. Plenty of quantitative information is still behind STM/STS data with no means of analyzing it. In order to extract rich information from the experimental data, we must know the real microscopic mechanism determining the tunneling current between the tip and the surface. But we do not have enough information about it.

For example, the distance between the tip and the surface is unknown quantitatively. The effect of the tip structure is not completely understood. In order to discuss STM/STS more quantitatively in atomic scale, it is needed to develop a theoretical method describing the tunneling current quantitatively. For that purpose, it is crucial to describe accurately the tail region of the surface wave function.

The purpose of this study is to develop a new theoretical method describing the tunneling current of STM/STS more quantitatively and to simulate STM/STS when the tip is far from the surface. Tsukada *et al.* [35] have developed a method of first-principle theoretical simulation of STM/STS with the use of LCAO representation of the wave function. The LCAO wave function, however, cannot be valid for the very tail part extending into the vacuum. So we try a new method in this thesis to describe the far tail regions effectively, which can be combined with realistic calculations of the surface and the tip electronic states. As a case study, we will discuss the Si(001) reconstructed surfaces, for which the STM/STS data introduced much information but also brought up several controversial problems.

§2.   Existing Theories of STM/STS

For the electron tunneling in STM, simple semi-classical theories will be appropriate as a first step for qualitative discussions. Traditional theories of the tunneling take the planer metal-insulator-metal (M-I-M) junction model [36,37]. The z-axis is perpendicular to the planer electrodes. The levels are treated as those of free electrons both in the tip and in the surface. Then the total current density, j_T, from the tip to the surface is written as

$$j_T = \frac{2e}{(2\pi)^2 \hbar} \int dE_z \iint d^2 k_{\parallel} [f(E) - f(E + ev)] T(E_z, k_{\parallel}), \qquad (1.1)$$

where

$$\begin{cases} E & = E_z + E(k_{\parallel}), \\ E(k_{\parallel}) & = \frac{\hbar^2}{2m} k_{\parallel}^2, \\ E_z & = \frac{\hbar^2}{2m} k_z^2. \end{cases} \qquad (1.2)$$

Here, $f(E)$ represents Fermi distribution function, $T(E_z, k_{\parallel})$ the transfer coefficient of the tunnel barrier, and v being the surface bias. The bottom of the valence band of the tip is taken as the origin of the energy. $(k_{\parallel}, k_z)$ is the wave vector of the free electron, parallel and perpendicular to the surface, respectively.

Within the 1D WKB approximation, the transfer coefficient is written as

$$T(E_z, k_{\parallel}) = \exp\left[-2 \int dz \sqrt{\frac{2m}{\hbar^2}(U(z) - E_z)}\right], \qquad (1.3)$$

where $U(z)$ is the tunnel barrier. If we approximate the barrier by a rectangular potential,

$$U(z) = E_F + \phi_0,$$

and assume that the work function is much larger than the bias potential, $\phi_0 \gg ev$, then the current density is approximately given by

$$j_T = v \frac{e^2}{\hbar} \frac{\kappa}{\pi^2 d} e^{-\kappa d}, \qquad (1.4)$$

where

$$\kappa = \sqrt{\frac{2m\phi_0}{\hbar^2}}, \qquad (1.5)$$

and d is the distance between the tip and the surface. Therefore, when the tip moves keeping the current constant, the tip approximately traces the contour of the surface defined by constant κd [1]. With work function, ϕ_0, of 5eV, a change of the tip position, δd, by 1Å leads to the change of the tunneling current up to one

order of magnitude. Moreover, with tunneling current of 1nA, surface bias of 1mV, and tip position 10Å, the radius of effective region where the current flows is about 5Å, according to eq.(1.4). Thus, qualitatively speaking, it would be able enough to measure the surface in atomic scale.

To proceed more accurately, there have been used two kinds of theoretical approaches. One is the semi-classical approach, which is based on the above formulation, eq.(1.1) [38–48].

Bono and Good used this approach [41]. They considered a system constructed by a planer surface and a semi-spherical tip attached to a parallel plane electrode, and calculated rigorously the image potential in such a configuration. The tunneling current was calculated at the tip top in terms of 1D WKB method. (Fig.1.2)

Lucas et al. [48] also used free electron approximation, but treated the transfer problem as a scattering problem more accurately by the Lippmann-Schwinger equation. They modeled the system by two parallel plane surfaces and a semi-spherical tip on one of the surfaces, and included the effect of the image potential. According to the use of cylindrical coordinates, the calculated current was quantized by the angular momentum quantity, m, and separated into two kinds of elements, j_z^m and J_ρ^m. They showed that only the element, $j_z^{m=0}$, is dominant, and the contributions from the other elements are less than 10%. They also showed that the tunneling current flows in the region of the radius of semi-spherical tip, and it was confirmed that the current flows only on the very narrow strip in the 3D space.

The advantage of this kind of approach is that the simplicity of the model enables us to treat the absolute value of the tunneling current analytically and numerically. In addition, it is also possible to treat the effect of the image potential and the electric field in the tunnel barrier. It is difficult, however, to include the real atomistic structure of the STM system constructed by a tip and a surface. Therefore it is difficult to discuss atomic scale images, and it remains a problem whether the semi-classical approximation is suitable or not for the real STM system.

The other kind of theoretical approach relies on Bardeen's equation. This equation is derived from the perturbation method in quantum mechanics [49]. We consider the system constructed by two electrodes, and the total electronic potential, V_{tot}, is divided into the left and the right part with its border surface, S. The left part of the potential, V_l, is zero in the right part, and the right part, V_r, is zero in the left part (Fig.1.3). Then the Hamiltonian is written as

$$H_{tot} = T + V_{tot},$$
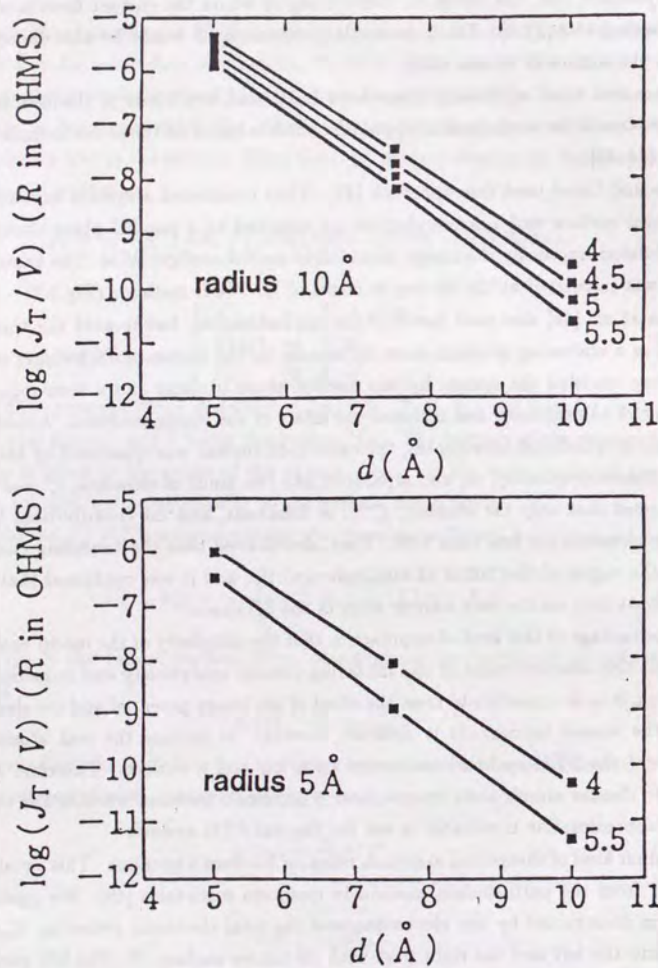
Figure 1.2: Calculation of the tunnel current by the 1D semi-classical method. (after Bono *et al.* [41]) The calculated curves for different sample work functions (unit eV) are presented simultaneously.

$$\begin{aligned}
&= \ T + V_l + V_r, \\
&= \ \begin{cases} H_l \ = \ T + V_l \quad (\mathbf{r} \in \text{left part}), \\ H_r \ = \ T + V_r \quad (\mathbf{r} \in \text{right part}). \end{cases}
\end{aligned} \tag{1.6}$$

Here we consider each eigenstate of H_l and H_r, $\psi_\mu(\mathbf{r})$ and $\psi_\nu(\mathbf{r})$ respectively, with their energy, E_μ and E_ν. Then, when the bias, v, is applied to the left part, the transition rate from the left to the right part, $P_{l \to r}$, can be calculated by the perturbation method as

$$P_{l \to r} = \frac{2\pi}{\hbar} \sum_{\mu\nu} |M_{\mu\nu}|^2 \delta(E_\mu - E_\nu + ev) f(E_\mu)(1 - f(E_\nu)), \tag{1.7}$$

where

$$\begin{aligned}
M_{\mu\nu} &= \frac{\hbar^2}{2m} \int_S d\mathbf{A} \cdot [\psi_\mu^*(\mathbf{r}) \boldsymbol{\nabla} \psi_\nu(\mathbf{r}) - \psi_\nu(\mathbf{r}) \boldsymbol{\nabla} \psi_\mu^*(\mathbf{r})], \\
&= \int d^3\mathbf{r} \, \psi_\mu^*(\mathbf{r}) V_r(\mathbf{r}) \psi_\nu(\mathbf{r}), \\
&= \int d^3\mathbf{r} \, \psi_\mu^*(\mathbf{r}) V_l(\mathbf{r}) \psi_\nu(\mathbf{r}).
\end{aligned} \tag{1.8}$$

The transition rate from the right to the left part is obtained in the same way. The total current from the right to the left part, I, is thus given by,

$$I = \frac{2\pi e}{\hbar} \sum_{\mu\nu} |M_{\mu\nu}|^2 \delta(E_\mu - E_\nu + ev)(f(E_\mu) - f(E_\nu)). \tag{1.9}$$

This equation is called Bardeen's equation. From the requirement of no current flow at zero bias, the Fermi energies of both parts must be coincident.

Tersoff and Hamann used this equation for STM system as early as 1984 [50,51]. They showed that if the probe wave function is spherical, the tunneling current is proportional to the LDOS of the surface at the center, $\mathbf{R}$, of the spherical tip model.

$$I \propto v \rho_s(\mathbf{R}; E_F). \tag{1.10}$$

In this case, the LDOS of the surface at the probe center around the Fermi energy is measured for a small bias region in the STM observation. By the same approach, it was speculated by many authors that the differential conductance is almost proportional to the LDOS of the surface,

$$\frac{dI}{dv} \propto \sigma_t(E_F) \rho_s(\mathbf{R}; E_F + ev), \tag{1.11}$$

where σ_t depends only on the tip character. This is used as the principle of STS [29].
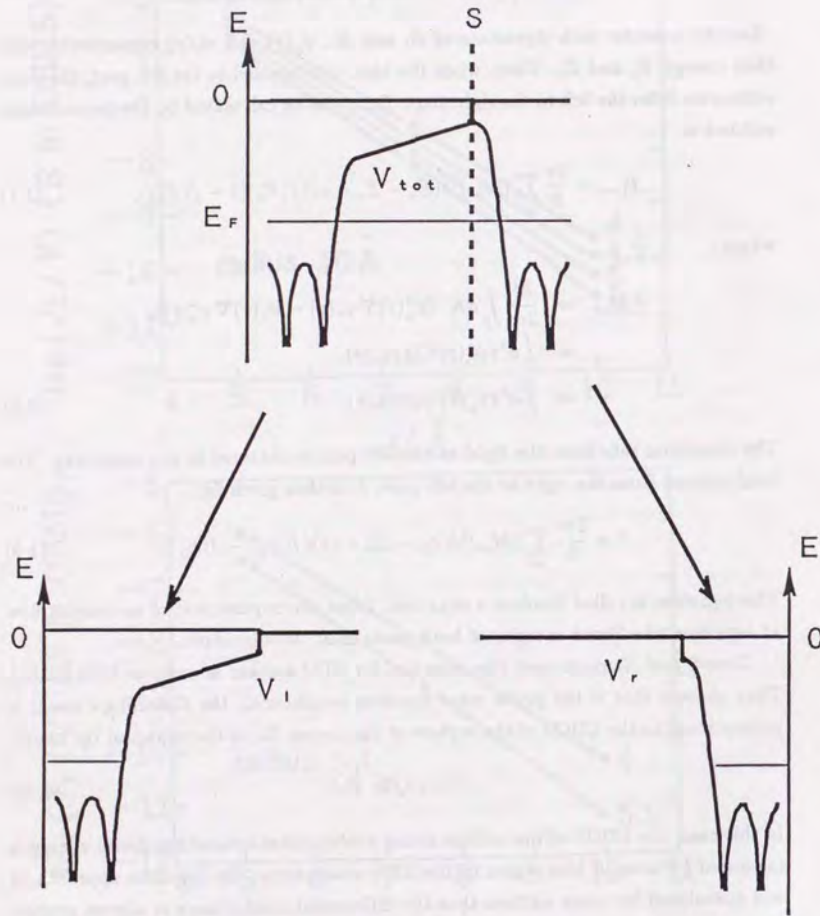
Figure 1.3: Schematic view of the approximation in deriving Bardeen's formula.

Applying these simple formulae eqs.(1.10) and (1.11), not only atomic images but also CDW images can be explained [52]. Tersoff indicated that the high resolution of the STM image of layer materials comes from the Fermi surface localized at the edges of Brillouin zone [53, 54]. The simple formulae such as eqs.(1.10) and (1.11) have been most convenient for providing a simple interpretation for STM images and STS spectra based on the microscopic electronic structure of the surface.

Using more exact formula eq.(1.9), Lang [55–59] showed how the difference of the chemisorbed atom on the surface is reflected on the corrugation of the STM image. When the tip atom is Na, the chemisorbed atom Na can be observed like a hill but the atom He is observed as a cave site. Furthermore, Chen [60] showed that the d orbitals of the tip cannot be neglected and the resolution of the image would be significantly improved by them. These studies clearly demonstrated the importance of the effect of the microscopic electronic states of the tip.

The systematic application of Bardeen's formula to the realistic STM system is studied by Tsukada and Shima [61]. They revealed the condition for obtaining atomistic image by the moment expansion method. Consider that the left part is the surface and the right is the tip. We introduce Green's function of the surface,

$$G_s(\mathbf{R}, \mathbf{R}'; E) = \sum_\mu \psi_\mu^*(\mathbf{R})\psi_\mu(\mathbf{R}')\delta(E - E_\mu). \tag{1.12}$$

Then the eq.(1.9) is rewritten as

$$
\begin{aligned}
I = {}& \frac{2\pi e}{\hbar} \int dE(f(E) - f(E + ev)) \\
& \times \sum_\nu \iint d^3\rho\, d^3\rho'\, \psi_\nu(\rho)\psi_\nu^*(\rho')V_\mathrm{l}(\rho)V_\mathrm{l}(\rho') \\
& \times G_s(\mathbf{R} + \rho, \mathbf{R} + \rho'; E)\delta(E - E_\nu + ev).
\end{aligned}
\tag{1.13}
$$

The surface wave functions decay at the tip position, so we can factor out the decay factor, $\gamma(\rho_z, E) = \exp(-\rho_z\sqrt{2m|E|/\hbar^2})$, from Green's function with the smooth part,

$$\mathcal{G}_s(\mathbf{R}, \mathbf{R}'; E) = G_s(\mathbf{R}, \mathbf{R}'; E)/\gamma(Z, E)/\gamma(Z', E). \tag{1.14}$$

Then the contribution to the integral mainly comes from the tip top region, and we expand the smooth part of Green's function around a fixed point of the tip, $\mathbf{R}$. The result is,

$$
\begin{aligned}
I = {}& \frac{2\pi e}{\hbar} \int dE(f(E) - f(E + ev)) \\
& \times \left[\sum_\nu \left| \int d^3\rho\, \psi_\nu(\rho)V_\mathrm{l}(\rho)\gamma(Z - \rho_z, E) \right|^2 \delta(E - E_\nu + ev) \right]
\end{aligned}
$$

$$\times \mathcal{G}_s(\mathbf{R}, \mathbf{R}; E)$$
$$+\frac{2\pi e}{\hbar} \int dE(f(E) - f(E + ev))$$
$$\times \left[\sum_\nu \left| \int d^3\rho \psi_\nu(\rho) V_l(\rho) \rho \gamma(Z - \rho_z, E) \right|^2 \delta(E - E_\nu + ev) \right]$$
$$\times \boldsymbol{\nabla}\boldsymbol{\nabla}\mathcal{G}_s(\mathbf{R}, \mathbf{R}; E)$$
$$+ \cdots .$$

$$(1.15)$$

In the above, the tip top center, $\mathbf{R}$, is determined by the condition so that the first order term of the moment expansion, which is proportional to $\boldsymbol{\nabla}\mathcal{G}_s(\mathbf{R}, \mathbf{R}; E)$, vanishes. If $\psi_\nu(\rho) V_l(\rho) \gamma(Z - \rho_z, E)$ is localized or spherical, the expansion can be approximated only by the first term. The approximation taking only the zeroth order term is equivalent to the Tersoff and Hamann's formula. Therefore, the Tersoff and Hamann's result is only accurate when the higher order terms in eq.(1.15) are negligible.

From eq.(1.15), the differential tunnel conductance is written as

$$\frac{dI}{dv} = \frac{2\pi e^2}{\hbar} \left[\sum_\nu \left| \int d^3\rho \psi_\nu(\rho) V_l(\rho) \gamma(Z - \rho_z, E_F - ev) \right|^2 \delta(E_F - E_\nu) \right]$$
$$\times \mathcal{G}_s(\mathbf{R}, \mathbf{R}; E_F - ev)$$
$$+\frac{2\pi e^2}{\hbar} \int dE(f(E) - f(E + ev))$$
$$\times \frac{\partial}{\partial E'} \left[\sum_\nu \left| \int d^3\rho \psi_\nu(\rho) V_l(\rho) \gamma(Z - \rho_z, E) \right|^2 \delta(E' - E_\nu + ev) \right]\Bigg|_{E'=E}$$
$$\times \mathcal{G}_s(\mathbf{R}, \mathbf{R}; E)$$
$$+\frac{2\pi e^2}{\hbar} \left[\sum_\nu \left| \int d^3\rho \psi_\nu(\rho) V_l(\rho) \rho \gamma(Z - \rho_z, E_F - ev) \right|^2 \delta(E_F - E_\nu) \right]$$
$$\times \boldsymbol{\nabla}\boldsymbol{\nabla}\mathcal{G}_s(\mathbf{R}, \mathbf{R}; E_F - ev)$$
$$+ \cdots .$$

$$(1.16)$$

When the bias is small or the tip electronic states do not change significantly with the level energy, the first term of eq.(1.16) is dominant and the differential conductance is almost proportional to the LDOS of the surface, $\rho_s(\mathbf{R}; E + ev)$. This is used as the principle of the STS, but we cannot always neglect the remaining terms of eq.(1.16) since the tip electronic states might have a significant energy dependence. In fact, the observations of the NDR shows the importance of the remaining terms. So, we must take care of this fact in analyzing the STS data [35].

First systematic calculations including realistic atomic models of the tip was initiated by Tsukada *et al.* [35]. Isshiki *et al.* [62] studied in detail the effect of the tip

in the STM images, and showed that the tip structure is sensitively reflected on the STM images of graphite. Kobayashi and Tsukada [63] studied the tip effect on STS spectra of graphite. They also studied the tip effect on STS spectra of the Si(111)/B with defect surface, and they showed that the NDR can be caused by the special tunnel active orbital on the tip [64].

Thus the approach based on Bardeen's formula can be used to elucidate the electronic structure of the sample surfaces from the information of STM/STS data. But, in the real numerical calculations, it is difficult to discuss the absolute value of the tunneling current far from the surface. The vacuum tails of the surface wave functions are needed to calculate the integral in eq.(1.8), since the potential $V_l(\mathbf{r})$ in eq.(1.8), which is zero in the surface, corresponds to the potential of the tip located $5 \sim 10\text{Å}$ far from the surface. The band calculation methods, however, represent well the surface wave functions only in the bulk or very close to the surface, but not well in the far distant region from the surface.

For example, Selloni *et al.* [65] calculated LDOS of graphite $2 \sim 4\text{Å}$ far from the surface by repeated slab band calculation in terms of the plane wave expansion with empirical local pseudopotential. But to describe the exponential decay of the tail, they must use huge number of plane waves. With 4-layers graphite and 4-layers vacuum, they used 705 plane waves (cut-off 13Ry) so as to describe the exponential decay of the (x,y) averaged charge density in accuracy of over five orders of magnitude. It would be difficult to apply this cut-off value to any sophisticated band calculations to obtain accurate LDOS in more distant region.

For the LCAO band calculation, the situation is the same. The vacuum tail of LCAO wave function is determined by an arbitrary chosen atomic basis set. Therefore, though the actual decay of the wave function is determined by its own energy, the decay of the LCAO wave function is characterized by the energy of the atomic orbital base. Thus, the vacuum tails are also poorly described in the LCAO method.

Therefore, in order to discuss STM/STS more quantitatively in atomic scale, it is needed to develop some new theoretical techniques along with Bardeen's formula so as to represent the vacuum tails of the wave functions accurately.

§3. Si(001) Reconstructed Surface

On the Si(001) reconstructed surface, STM/STS observation have played an important role to analyze the structure of the reconstruction. In this surface, many kinds of reconstructions have been proposed; (2×1) [66–69], $p(2\times2)$, $c(4\times2)$ [70–76], $c(4\times4)$

[77], and also $(2 \times n)$ $(6 \leq n \leq 10)$ [78–79]. Appearance of these reconstructions depend on the way of preparation of the sample as well as the temperature. And also many kinds of the structural models have been proposed, which are grouped as dimer models [80–88], conjugated chain models [89–91], and vacancy models [66, 73, 74, 92]. Our understanding of this surface was incomplete before the observation of the STM image. Hamers *et al.* [88] first clearly observed the Si(001) surface by STM (Fig.1.5). They observed at room temperature the dimer structures on the Si(001) (2×1) surface as well as randomly distributed vacancies. They observed p(2×2) domains as well as c(4×2) domains around a defect region, but mostly (2×1) symmetric dimer arrays in defect-free regions. The real imaging of this surface revealed a variety of the reconstructions.

(2×1) non-buckled dimer observed in defect-free regions, however, contradicts with other experimental results such as low energy electron diffraction (LEED), ion-scattering, and helium diffraction studies, which supported buckled dimer structure. Moreover the photoemission studies [94–98] have shown that the surface band has a semiconducting feature, but according to theoretical studies, the symmetric dimer model has the metallic feature and the buckling of the dimer leads to the semiconducting one. The reason why the STM images show symmetric dimer structure is puzzling. There are two possibilities, either the non-buckled image of STM actually corresponds to the symmetric dimer, or not. If the latter is true, the following mechanisms could be proposed for this as; (a) the STM tip moves the dimer atom when the tip comes above the atom. (b) the STM image of the asymmetric dimer structure looks like symmetric dimer and the two structure cannot be distinguished from the image. (c) the buckled dimer oscillates thermally like a seesaw and the time-averaged structure of the oscillating dimer is observed in STM. The answer with any conclusive evidence has not been given, yet.

Figs.1.6, 1.7, and 1.8 show recent improved data of STM/STS in the Si(001) (2×1) region [99]. A characteristic feature is that we can recognize each atom in the STM image for the positive surface bias. For the image at the negative surface bias, dimer is observed as a bean-like image again as if the dimer bridge is highlighted. The maximum corrugation is about 0.8Å along the bridge, and there is surely a deeper node at the middle of the dimer bridge for the positive surface bias. From the STS data, we can recognize four major structures in the spectrum originated from the surface bands. One large structure is found in $V = -0.9$V, and broader three structures are found in $V = +0.3$V, $+0.7$V and $+1.4$V. These data were interpreted
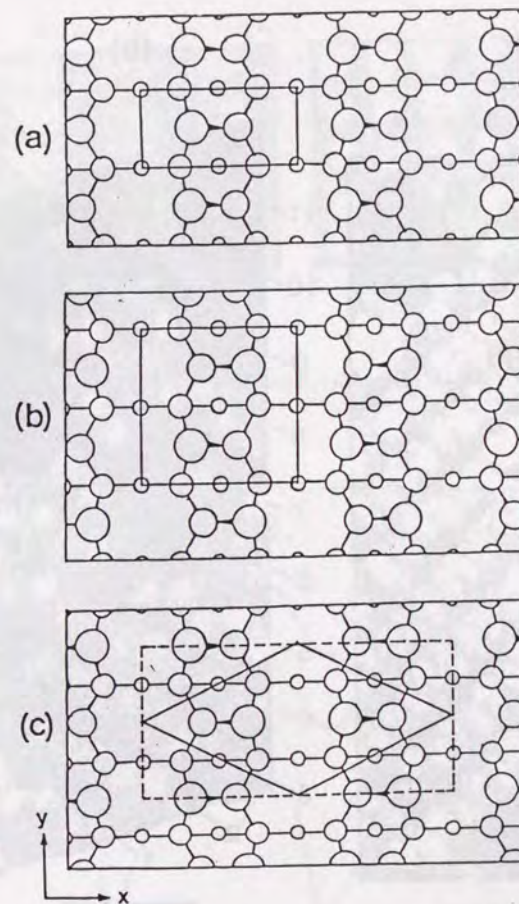
Figure 1.4: Variation of dimer structure of Si(001). (a) (2×1), (b) p(2×2), (c) c(4×2) (broken line represents the unit cell used in Chapter 3). (after Zhu *et al.* [93])
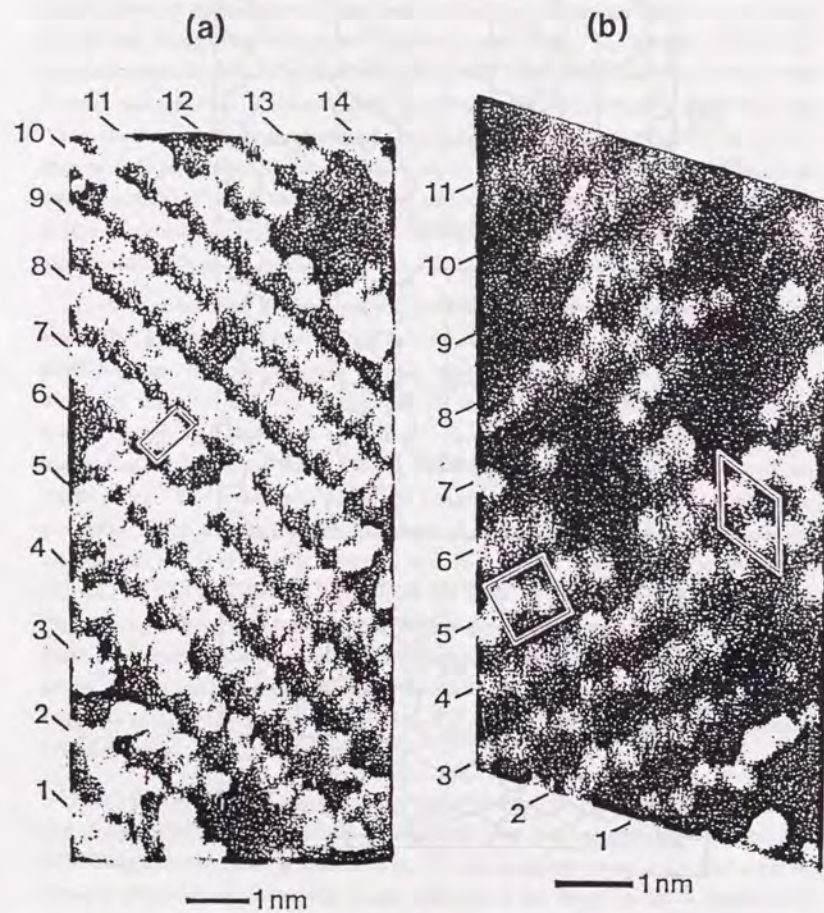
Figure 1.5: STM image on Si(001) (after Hamers *et al.* [88]) (a) (2×1) structure, (b) p(2×2) and c(4×2) structures.

Figure 1.6: STM images of (2×1) are taken at (a) surface bias −2V, (b) +1.2V. (after Hamers *et al.* [99])

Figure 1.7: Tip motions of (2×1) region are drawn. (A) surface bias −2V, (B) +1.2V, (C) NH₃-dosed −2V. (after Hamers *et al.* [99])

Figure 1.8: STS spectrum averaged in the (2×1) region. (A) clean Si(001) (B) NH$_3$ dosed. (after Hamers *et al.* [99])

simply by using eqs.(1.10) and (1.11), but have not been analyzed quantitatively by any theoretical simulations, yet. Ohnishi and Tsukada [100] studied this surface by the use of the cluster model both for the tip and for the surface, but their cluster model used for the surface is not appropriate enough to discuss the STM images and the STS spectra, because the surface states construct surface bands which have dispersion relation. Therefore, it would be interesting to apply our new method to this surface and analyze the experimental data of STM/STS.

Chapter 2

Method for the Theoretical Simulation of STM/STS

§1. Method of the Simulation

In this chapter, we describe our method of the simulation of STM/STS. The theoretical simulations of STM/STS have been studied by several authors as mentioned in Chapter 1 since the experimental element was developed by Binnig and Rohrer. In order to simulate the local microscopic tunneling current of STM/STS, the most convenient approach is to use Bardeen's equation of tunneling current [49],

$$I(\mathbf{R}, v) = \frac{2\pi e}{\hbar} \sum_{\mu\nu} |M_{\mu\nu}(\mathbf{R})|^2 [f(E_\mu) - f(E_\nu)]\delta(E_\mu - E_\nu + ev). \tag{2.1}$$

This equation is derived by dividing the total system into two systems, the left-hand electrode and the right-hand electrode. If the two systems are enough separated by the vacuum potential barrier, the perturbational treatment is valid and leads to this equation. Here, E_μ represents the energy of the μ-th eigenstate of the left-hand-side system, and E_ν represents that of the ν-th eigenstate of the right-hand-side. $f(E)$ is the Fermi distribution function, and v is the bias of the right-hand-side referred to the left-hand-side. The positive sign of the current, $I(\mathbf{R})$, corresponds to the flow from right to left. The tunneling matrix element, $M_{\mu\nu}(\mathbf{R})$, is defined as

$$M_{\mu\nu}(\mathbf{R}) = \langle \psi_\mu(\mathbf{r})|V_l(\mathbf{r} - \mathbf{R})|\psi_\nu(\mathbf{r} - \mathbf{R})\rangle, \tag{2.2}$$

where $\psi_\mu(\mathbf{r})$ is the wave function of the μ-th eigenstate of the left-hand-side system, $\psi_\nu(\mathbf{r})$ that of the ν-th eigenstate of the right-hand-side system, and $V_l(\mathbf{r})$ is the one body electronic potential of left-hand-side system, which is zero in the right-hand-side. $\mathbf{R}$ denotes the position of the right-hand-side system relative to the left-hand-side

system. Eq.(2.1) contains information of the local electronic states of both systems. This character is convenient for simulating STM/STS.

We assume that the left-hand-side system corresponds to the surface and the right-hand-side system to the tip. In order to evaluate the equation, eq.(2.1), we need the wave functions of both systems and the potential of the tip system. Kobayashi *et al.* [63] calculated the wave functions of the surface system by DV-Xα-LCAO-band method, and the wave functions and the potential of the tip system by DV-Xα-LCAO-cluster method. These results were approximately used in order to evaluate eq.(2.1). The atomic orbital basis and the atomic potentials were fitted by the linear combination of Gaussian type orbitals (GTO's), and the integral in the transfer matrix element was evaluated analytically. In this way, they could evaluate eq.(2.1) straightforwardly with the effect of a realistic tip electronic structure being included.

However, we must notice that the STM tip position is believed to be $5 \sim 10$Å far from the surface. The potential $V_t(\mathbf{r})$ is the tip potential, thus the region around the tip most contributes to the integral in eq.(2.2). In such a long distance, the surface wave functions decay so much that the LCAO description for the tails of the surface wave functions may not be so good. This is because the tail of the LCAO wave function is determined by the arbitrarily chosen atomic basis set, which describes well the closer regions to the core but not necessarily good for the region far apart from the core. For example, we assume one level consists of $2s$ and $2p_z$ atomic orbitals. Far from the core, the vacuum tail of the level is characterized by $2p_z$ orbital because of the difference of orbital's energies. But it does not represent the real situation. The vacuum tail must be characterized not by the energy of the atomic orbital base but by its own eigenenergy. In addition, when the tip position is moved far from the surface, the number of the AO's which must be taken into account in the tunneling matrix element increase enormously. From these constraints of the method, Kobayashi *et. al.* put the tip at the distance closer than 5au (~ 2.6Å) from the surface for most of the cases.

To avoid the above restrictions, we must break through the constraints of the LCAO approximation. One possibility is to use the plane wave expansion. In the region outside the surface, the potential decays to zero, so the plane wave approximation for the parallel direction to the surface will be effective in this region. But, in this approximation, we need too many basis to represent the exponentially damping behavior of wave function toward the vacuum region [65]. In addition, the width of vacuum layer is also limited. Thus, this approach would not be effective either.

The virtue of the plane wave basis outside the surface is broken only in the perpendicular direction to the surface. In the 2D space parallel to the surface, they are effective enough. Thus, it looks appropriate to represent the wave functions in the direction parallel to the surface by the plane waves with some decaying factor in the perpendicular direction to the surface. But, this breaks the 3D symmetry in the formalism and leads to tedious procedure for the band calculation. So, we take this method only in the region outside the surface, and we take the ordinary band calculation method, say, DV-Xα-LCAO-band method inside the surface. In the self-consistent field (SCF) band calculation, it is not necessary to take into account far outside region of the surface, because their contribution to the self consistent potential is small enough compared with that inside the surface. The basic idea for calculating the vacuum tail of the surface wave functions is the same as that proposed by Tersoff [101], but our method is more practical in numerical calculations.

Such a continuation method could be applied to the plane wave band calculation method for the semi-infinite surface. But, because the calculated wave functions have crystal momentum perpendicular to the surface, the effect of the incident wave belonging to one band would be reflected on some waves belonging to the other bands, when several bands go across the same energy. Then it would be difficult to continue the waves at the boundary. Besides, we are interested in checking the validity of the LCAO approximation in STM/STS simulation. Therefore, here we decide to use DV-Xα-LCAO-band method. The details of our idea will be described in the following sections. And the difference between our method and the ordinary LCAO method will be also discussed later.

§2. Method of Calculating the Tail of the Surface Wave Function

In this section, we show how we calculate the tail of the wave function of the surface. In the LCAO approximation, the wave function is well represented around the region of atomic radius from the core, but not so well far from the core. In the vacuum, the 2D plane wave basis with a damping profile will represent wave functions much better than LCAO basis. So we can represent the wave functions in the surface by the LCAO basis, and those far from the surface by the plane wave basis with a damping profile. Thus, we divide the region from the surface to the vacuum into three parts (Fig.2.1); one is the surface region, where we represent the wave functions by the LCAO basis.
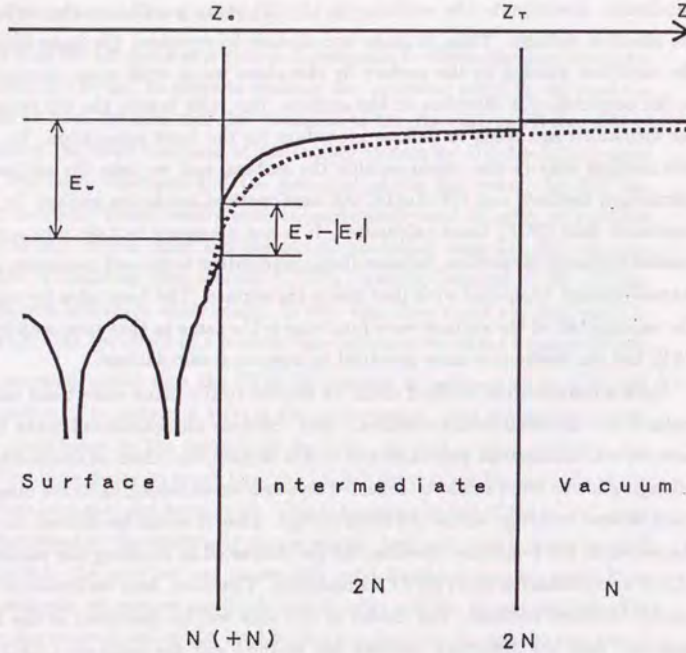
Figure 2.1: Schematic draw of dividing the region. The number of conditions and parameters to determine are also described.

Another is the vacuum region, where we represent the wave function by the 2D plane wave basis with damping profile. The other is the intermediate region, where we can represent the wave function neither by the LCAO basis nor by the plane wave basis. Now, the problem is how to continue the wave functions in the surface and far from the surface through the intermediate region.

§2.1 Wave Function in the Surface Region

The electronic structure is calculated self-consistently in the surface region, without considering the existence of the division of the space, as mentioned above. We briefly

describe the method of DV-Xα-LCAO-band calculation here, but the detail would be found in Shima's article [102] or Zunger and Freeman's one [103]. In the surface region, the wave function is represented by the LCAO approximation as follows.

$$\psi_s(\mathbf{k}_{\parallel}, n; \mathbf{r}) = \frac{1}{\sqrt{N}} \sum_{m,a} \sum_{\alpha \in a} e^{i\mathbf{k}_{\parallel} \cdot (\mathbf{R}_{\parallel a} + \mathbf{R}_{\parallel m})} C_\alpha(\mathbf{k}_{\parallel}, n) \phi_\alpha(\mathbf{r}_{\parallel} - \mathbf{R}_{\parallel a} - \mathbf{R}_{\parallel m}, z - z_a). \quad (2.3)$$

Here $(\mathbf{R}_{\parallel a}, z_a)$ is the position of the a-th atom in the unit cells, and $(\mathbf{R}_{\parallel m}, 0)$ the m-th lattice vector. $\phi_\alpha(\mathbf{r}_{\parallel}, z)$ represents the wave function of the α-th atomic orbital. N is the number of unit cell. $C_\alpha(\mathbf{k}_{\parallel}, n)$ is the LCAO coefficient of the α-th atomic orbital, which must be determined by the following secular equation,

$$\sum_{\alpha'} H_{\alpha,\alpha'}(\mathbf{k}_{\parallel}) C_{\alpha'}(\mathbf{k}_{\parallel}, n) = E(\mathbf{k}_{\parallel}, n) \sum_{\alpha'} S_{\alpha,\alpha'}(\mathbf{k}_{\parallel}) C_{\alpha'}(\mathbf{k}_{\parallel}, n), \quad (2.4)$$

where

$$
\begin{aligned}
H_{\alpha,\alpha'}(\mathbf{k}_{\parallel}) &= \sum_m e^{i\mathbf{k}_{\parallel} \cdot (\mathbf{R}_{\parallel m} - \mathbf{R}_{\parallel a} + \mathbf{R}_{\parallel a'})} \\
&\quad \times \langle \phi_\alpha(\mathbf{r}_{\parallel} - \mathbf{R}_{\parallel a}, z - z_a) | H | \phi_{\alpha'}(\mathbf{r}_{\parallel} - \mathbf{R}_{\parallel a'} - \mathbf{R}_{\parallel m}, z - z_{a'}) \rangle, \quad (2.5) \\
S_{\alpha,\alpha'}(\mathbf{k}_{\parallel}) &= \sum_m e^{i\mathbf{k}_{\parallel} \cdot (\mathbf{R}_{\parallel m} - \mathbf{R}_{\parallel a} + \mathbf{R}_{\parallel a'})} \\
&\quad \times \langle \phi_\alpha(\mathbf{r}_{\parallel} - \mathbf{R}_{\parallel a}, z - z_a) | \phi_{\alpha'}(\mathbf{r}_{\parallel} - \mathbf{R}_{\parallel a'} - \mathbf{R}_{\parallel m}, z - z_{a'}) \rangle. \quad (2.6)
\end{aligned}
$$

We evaluate the matrix elements by the DV method. The Coulomb and the exchange-correlation potentials in the Hamiltonian are self-consistently determined by the standard iteration procedure. The exchange-correlation potential is chosen as the Xα potential, with the value of α equal to 0.7. We treat all electrons in the unit cell including the core electrons, and the minimal basis set for the Si atom is 1s~3s, 2p, and 3p orbital, which are self-consistently calculated numerically in each iteration step. The surface is replaced by the isolated slab, which has only 2D periodicity.

§2.2 Wave Function in the Vacuum Region

In the vacuum region, we simply assume that the electronic potential vanishes. Then the wave functions are free waves along the surface and must decay from the surface into the vacuum. The wave function which has a momentum parallel to the surface, $\mathbf{k}_{\parallel}$, is written as follows.

$$\psi_v(\mathbf{k}_{\parallel}; \mathbf{r}) = A e^{i\mathbf{k}_{\parallel} \cdot \mathbf{r}_{\parallel}} e^{-\kappa(E, \mathbf{k}_{\parallel})z}, \quad (2.7)$$

where

$$\kappa(E, \mathbf{k}_{\parallel}) = \sqrt{\mathbf{k}_{\parallel}^2 - \frac{2m}{\hbar^2} E}. \quad (2.8)$$

Here we take the z-axis perpendicular to the surface, and the direction into the vacuum is taken as that of plus z. In this region, any linear combinations of this kind of wave functions, which have the same energy, E, can be the eigenstates, and the coefficients of combination are determined by the boundary condition at the dividing surface with the intermediate region.

§2.3 Wave Function in the Intermediate Region

In the intermediate region, we use the 2D Fourier transformed representation along the surface. The 2D Fourier transformed representation of the Schrödinger equation can be written as follows;

$$E\psi_m(\mathbf{k}_\parallel, n; \mathbf{G}_\parallel, z) = \frac{\hbar^2}{2m}(\mathbf{k}_\parallel + \mathbf{G}_\parallel)^2 \psi_m(\mathbf{k}_\parallel, n; \mathbf{G}_\parallel, z) - \frac{\hbar^2}{2m}\frac{\partial^2}{\partial z^2}\psi_m(\mathbf{k}_\parallel, n; \mathbf{G}_\parallel, z)$$
$$+ \sum_{\mathbf{G}'_\parallel} V(\mathbf{G}_\parallel - \mathbf{G}'_\parallel, z)\psi_m(\mathbf{k}_\parallel, n; \mathbf{G}'_\parallel, z), \qquad (2.9)$$

where

$$\psi_m(\mathbf{k}_\parallel, n; \mathbf{r}) = \sum_{\mathbf{G}_\parallel} e^{i(\mathbf{k}_\parallel + \mathbf{G}_\parallel)\cdot\mathbf{r}_\parallel}\psi_m(\mathbf{k}_\parallel, n; \mathbf{G}_\parallel, z), \qquad (2.10)$$

$$V(\mathbf{r}) = \sum_{\mathbf{G}_\parallel} e^{i\mathbf{G}_\parallel\cdot\mathbf{r}_\parallel}V(\mathbf{G}_\parallel, z). \qquad (2.11)$$

This is a coupled differential equation. Each element of 2D Fourier transformation of the wave function, $\psi_m(\mathbf{k}_\parallel, n; \mathbf{G}_\parallel, z)$, is correlated with each other and varies with the distance from the surface. The 2D Fourier components of the potential, $V(\mathbf{G}_\parallel, z)$, outside the surface may decay into the vacuum. The components with larger $\mathbf{G}_\parallel$'s may decay more quickly, and only the $\mathbf{G}_\parallel = (0, 0)$ component survives far into the vacuum. So, in the region far enough into the vacuum, the coupled equation is decoupled and the wave functions take the free wave form.

In order to solve eq.(2.9), the boundary condition must be determined. On the boundary with the vacuum region, $z = z_v$, the each element, $\psi_m(\mathbf{k}_\parallel, n; \mathbf{G}_\parallel, z)$, continues to the corresponding damping wave. The boundary condition is,

$$\frac{\partial \log \psi_m}{\partial z}(\mathbf{k}_\parallel, n; \mathbf{G}_\parallel, z_v) = -\kappa(E, \mathbf{k}_\parallel + \mathbf{G}_\parallel), \qquad (2.12)$$

$$\psi_m(\mathbf{k}_\parallel, n; \mathbf{G}_\parallel, z_v) = \psi_v(\mathbf{k}_\parallel, n; \mathbf{G}_\parallel, z_v). \qquad (2.13)$$

On the boundary with the surface region, $z = z_c$, each element, $\psi_m(\mathbf{k}_\parallel, n; \mathbf{G}_\parallel, z)$, continues to the corresponding element of the surface wave function represented by

the LCAO. The total number of boundary conditions is three times the number of the 2D Fourier elements, that is $3N$, and we already took $2N$ of them for the boundary conditions on the vacuum side. Thus we can take N boundary conditions on the surface side, and the conditions are conveniently taken as follows.

$$\psi_s(\mathbf{k}_\parallel, n; \mathbf{G}_\parallel, z_c) = \psi_m(\mathbf{k}_\parallel, n; \mathbf{G}_\parallel, z_c). \qquad (2.14)$$

Now, the tail of the wave functions in the vacuum region is written as

$$\psi_v(\mathbf{k}_\parallel, n; \mathbf{r}) = \sum_{\mathbf{G}_\parallel} e^{i(\mathbf{k}_\parallel + \mathbf{G}_\parallel)\cdot\mathbf{r}_\parallel} D(\mathbf{k}_\parallel, n; \mathbf{G}_\parallel)e^{-\kappa(E(\mathbf{k}_\parallel,n),\mathbf{k}_\parallel + \mathbf{G}_\parallel)z}. \qquad (2.15)$$

There remains the conditions of the continuation of the differentials of the wave function perpendicular to the boundary, but we have already taken enough conditions, so these conditions are neglected here. Such a situation occurs because the wave functions and energies of the levels on the surface are already determined by the isolated slab calculation. Generally speaking, the jump of the derivative of the wave function changes the energy of the connected total wave function. The change of energy, δE, is approximately represented as

$$\delta E = \Re\left[\frac{\hbar^2}{m}\int_{z=z_c} d^2\mathbf{r}_\parallel \psi_s^*\left(\frac{\partial}{\partial z}\psi_m - \frac{\partial}{\partial z}\psi_s\right)\right]. \qquad (2.16)$$

The method proposed above would lead to a reasonable result with careful calculation, if only δE is small enough compared with the band width. It is necessary to check the value of δE in the calculation.

In the actual calculation, the reciplocal elements of the wave function are taken into account if the absolute value of the reciplocal lattice vector is smaller than the cut-off, G_{c1}. In addition, we introduce one more cut-off value for the reciplocal lattice elements, because of the numerical problem in the integration of the coupled differential equations, eq.(2.9). We decouple the reciplocal elements from the coupled equation, the absolute value of whose reciplocal vector is larger than the cut-off, G_{c2}, eq.(2.9). Moreover we consider only the $\mathbf{G}_\parallel = (0, 0)$ reciplocal element of the potential in solving those reciplocal elements of the wave function. The elements are treated accurately along eq.(2.9), the absolute value of whose reciplocal vector is smaller than the cut-off, G_{c2}.

§2.4 Potential in the Intermediate Region

In the intermediate region, eq.(2.9) must be solved with the boundary conditions, eqs.(2.12), (2.13) and (2.14). To solve this equation, we must determine the potential,

$V(\mathbf{r})$. The potential far from the surface is usually divided into two parts; the statistic Coulomb part and the image potential part [104]. To determine the potential outside the surface, we must obtain these two parts numerically with good accuracy, but this is not easy to do.

The static Coulomb part comes from the microscopic dipole layer around the surface, and extends both into bulk and vacuum. Especially the tail of the dipole layer is important to determine the Coulomb part, and a small change of the charge density at the tail of the dipole layer induces a relatively large change in the Coulomb part. Thus determination of this part requires very sophisticated treatment, and it is very difficult to carry it out numerically. In addition, LCAO approximation does not have enough freedoms to describe the dipole layer because of the localized character of the AO basis.

The image potential part is also difficult to determine. The correlation potential in the region far from the surface is nothing more than the image potential. In this region, the correlation potential becomes long range and non-local, so the local density approximation (LDA) for the exchange-correlation potential is not suitable there. Essentially manybody problem treatment is necessary for the determination of this image potential. Therefore, the potential outside the surface is difficult to determine within enough accuracy. So we treat the potential of the intermediate region by a model.

In this paper, we simply take the potential calculated by the DV-Xα-LCAO-band method to solve the eq.(2.9) as the real potential in the surface region (Fig.2.1). In the DV-Xα-LCAO-band method, the calculated work function, *i.e.* minus of the Fermi energy relative to the vacuum energy, is generally small compared with the experimental one. We introduce a step-function-like jump of the potential at the surface-intermediate boundary, so that the Fermi energy position relative to the vacuum is equal to the experimental work function. So, in the intermediate region, the potential is assumed to be same as that calculated by the DV-Xα-LCAO-band method except for a shift of the origin of energy. We put the potential as zero in the vacuum region.

To describe the potential outside the surface realistically, it would be better to use some empirical potential, which smoothly decays and have the form as $-e/\epsilon 2(z - z_0)$ far from the surface. It is possible for us to take such a potential barrier, but our adopted model potential would be good enough as a first approximation. The difference of the potentials is included only in the $\mathbf{G}_\parallel = (0, 0)$ element, so the calculated

image would not be influenced by this approximation. The absolute value of the calculated tunneling current, however, would be influenced, and the obtained current would be underestimated because of the rapid decay of the barrier potential.

The 2D Fourier transform of the potential, $V(\mathbf{G}_\parallel, z)$, used in eq.(2.9) is calculated from the potential, $V(\mathbf{r})$, as follows.

$$V(\mathbf{G}_\parallel, z) = \frac{1}{\Omega_0} \int_{\Omega_0} d^2\mathbf{r}_\parallel e^{-i\mathbf{G}_\parallel \cdot \mathbf{r}_\parallel} V(\mathbf{r}_\parallel, z), \qquad (2.17)$$

where Ω_0 is the area of the surface unit cell.

§2.5 Determination of the Positions of Boundaries of the Intermediate Region

The division of the space into the three parts is artificial, and there are no clear boundaries in the real system. In choosing the boundaries, we must consider the meaning of the approximations in each region.

In the vacuum region, the potential variation can be neglected, and it is possible that we regard the region as a free space. So, if the depth of the potential is very small there compared with that of the work function, then such a region can be chosen as the vacuum region. The boundary between the vacuum and the intermediate region can be determined anywhere, if only this condition is satisfied. But to avoid huge computational time, the boundary should not be taken at so distant region from the surface. The criterions would be as follows; (1) the 2D Fourier elements of potential except for the $\mathbf{G}_\parallel = (0, 0)$ element are negligibly small compared with the $\mathbf{G}_\parallel = (0, 0)$ element, (2) the $\mathbf{G}_\parallel = (0, 0)$ element is small enough compared with the work function, (3) the classical turning point for the Fermi level is sufficiently inside the boundary so that the wave functions almost decay.

The boundary between the surface and the intermediate region has two meanings. One is that the potential jumps up there in order to reproduce the height of the potential barrier. Its choice is equivalent to the choice of the model of the tunneling barrier potential. The real potential smoothly decay from the surface to the vacuum, and its vacuum tail has the form, $-e/\epsilon 2(z - z_0)$. It would be better to determine the boundary position with considering the real behavior of the barrier potential.

The other is that the wave functions of the intermediate region and the surface region are connected there. To avoid insufficient description of the tail of the LCAO wave function, it is better to choose the position of the boundary nearest to the outermost atoms of the surface. Formally speaking, solving eq.(2.9) is equivalent to

solving the secular equation, eq.(2.5), and we can take the boundary anywhere in the surface. But, from the viewpoint of numerical calculation, we cannot include so many reciplocal lattice vectors, $\mathbf{G}_\parallel$. Therefore the boundary plane should not be chosen at very close position to the surface, where description of the wave function requires a large number of $\mathbf{G}_\parallel$'s.

These two factors must be considered when the position of the surface-intermediate boundary is determined.

§3. Wave Functions of the Tip

The microscopic nature of the tip has an important effect on STM/STS. The NDR is one peculiar example demonstrating it. In the case of Si(111) $\sqrt{3} \times \sqrt{3}$/B system, STS experiments show the NDR on the defect site, where a boron atom is replaced by a silicon atom [34]. This could not be explained without the specific feature of the tip electronic state [63]. If we ignore the energy dependence of the DOS of the tip, the NDR should not be caused, since the differential conductance is proportional to the surface LDOS at the probe point of the tip in this approximation. To perform a realistic theoretical simulation, it is most crucial to include the microscopic nature of the tip.

Here we describe the method to include the effect of the tip. We model the tip as a cluster, and calculate the electronic structure of the tip by DV-Xα-LCAO-cluster method [105]. The Coulomb potential and the exchange-correlation potential are calculated by the standard self-consistent field procedure, which is almost the same as the calculation of the electronic structure of the surface. α is chosen as 0.7 and all electrons in the cluster are considered. The minimal basis set for the W is 1s~6s, 2p~5p, 3d~5d, and 4f orbital, which are self-consistently calculated for each iteration step.

We fit the numerical atomic orbital basis and the atomic potential by linear combinations of GTO's;

$$r^l R_{nl}^a(r) = \sum_i A_{nl,i}^a e^{-B_{nl,i}^a r^2}, \tag{2.18}$$

$$r V^a(r) = \sum_i A_{V,i}^a e^{-B_{V,i}^a r^2}, \tag{2.19}$$

where $R_{nl}^a(r)$ is the radial part of the n, l type atomic orbital on the a-th atom, and $V^a(r)$ is the spherical averaged atomic potential of the a-th atom. In case of fitting the atomic orbitals, we check their norms to be equal to one.

When the tip position is deep inside the vacuum region, we can calculate the transfer matrix elements with fitted Gaussian parameters.

$$M_{(\mathbf{k}_\parallel, n), \nu}(\mathbf{R}) = \sum_{\mathbf{G}_\parallel} D(\mathbf{k}_\parallel, n; \mathbf{G}_\parallel) \sum_a \sum_{\alpha \in a} C_\alpha^\nu \sum_i A_{\alpha,i}^a \sum_{a',i'} A_{V,i'}^{a'} J(\mathbf{k}_\parallel, n, \mathbf{G}_\parallel, \nu, a, \alpha, i, a', i'), \tag{2.20}$$

where

$$\begin{aligned} J(\mathbf{k}_\parallel, n, \mathbf{G}_\parallel, \nu, a, \alpha, i, a', i') &= \int d^2 \mathbf{r}_\parallel e^{i(\mathbf{k}_\parallel + \mathbf{G}_\parallel) \cdot \mathbf{r}_\parallel - \kappa(E(\mathbf{k}_\parallel, n), \mathbf{k}_\parallel + \mathbf{G}_\parallel) z} \\ &\quad \times \mathcal{Y}_{lm}\left(\overline{\mathbf{r} - \mathbf{R}_a - \mathbf{R}}\right) |\mathbf{r} - \mathbf{R}_a - \mathbf{R}|^l \\ &\quad \times e^{-B_{\alpha,i}^a (\mathbf{r} - \mathbf{R}_a - \mathbf{R})^2} \frac{e^{-B_{V,i'}^{a'}(\mathbf{r} - \mathbf{R}_{a'} - \mathbf{R})^2}}{|\mathbf{r} - \mathbf{R}_{a'} - \mathbf{R}|}. \end{aligned} \tag{2.21}$$

α denotes (n, l, m) and ν denotes the index of the tip level. The 3D integration in eq.(2.21) can be reduced to 1D integration as shown in Appendix.

Now we can calculate the tunneling current from eq.(2.1). But the levels of the tip are discrete, not continuum, because we model the tip by a finite cluster. Because the real tip is one part of macroscopic system with a continuum spectrum, we must use some method which reproduces continuum spectrum. We replace the δ function DOS, $\delta(E - E_\nu)$, of each level by the lorenzian function, $(\Delta/\pi)/[(E - E_\nu)^2 + \Delta^2]$. This procedure is justified by Green's function method, though we have not practiced any accurate calculations based on it, yet. The value of the width would be evaluated from the bulk band calculation or other ways. Then the tunneling current has the form,

$$\begin{aligned} I(\mathbf{R}, v) &= \frac{2\pi e}{\hbar} \sum_n \frac{\Omega_0}{(2\pi)^2} \int_{BZ} d^2 \mathbf{k}_\parallel \left[f(E(\mathbf{k}_\parallel, n)) - f(E(\mathbf{k}_\parallel, n) + ev) \right] \\ &\quad \times \sum_\nu |M_{(\mathbf{k}_\parallel, n), \nu}(\mathbf{R})|^2 \frac{\Delta/\pi}{(E(\mathbf{k}_\parallel, n) + ev - E_\nu)^2 + \Delta^2}, \end{aligned} \tag{2.22}$$

and the differential conductance is represented as

$$\begin{aligned} \frac{dI}{dv}(\mathbf{R}, v) &= \frac{2\pi e^2}{\hbar} \sum_n \frac{\Omega_0}{(2\pi)^2} \int_{BZ} d^2 \mathbf{k}_\parallel \left[f(E(\mathbf{k}_\parallel, n)) - f(E(\mathbf{k}_\parallel, n) + ev) \right] \\ &\quad \times \sum_\nu |M_{(\mathbf{k}_\parallel, n), \nu}(\mathbf{R})|^2 \frac{(-2\Delta/\pi)(E(\mathbf{k}_\parallel, n) + ev - E_\nu)}{\left[(E(\mathbf{k}_\parallel, n) + ev - E_\nu)^2 + \Delta^2 \right]^2} \\ &\quad + \frac{2\pi e^2}{\hbar} \sum_n \frac{\Omega_0}{(2\pi)^2} \int_{BZ} d^2 \mathbf{k}_\parallel \delta(E(\mathbf{k}_\parallel, n) + ev - E_F) \\ &\quad \times \sum_\nu |M_{(\mathbf{k}_\parallel, n), \nu}(\mathbf{R})|^2 \frac{\Delta/\pi}{(E(\mathbf{k}_\parallel, n) + ev - E_\nu)^2 + \Delta^2}, \end{aligned} \tag{2.23}$$

where E_F is the Fermi energy of the surface. Here we shift the energy level of the tip so that the Fermi energy of the tip coincides with that of the surface. This is required by the zero current condition at zero bias. The theoretical simulation of STM/STS hereafter will be performed with eqs.(2.22) and (2.23). According to Kobayashi *et al.* and Isshiki *et al.*, the simulated STM image does not depend on the value of the width, Δ, but the STS spectrum does.

Usually, STM observation is the constant current image (corrugation image), though the constant height image (current image) is easier to calculate theoretically. So we use simple approximation to obtain the constant current image. If the tip height moves by a small value, Δz, then the change of the current, ΔI, is related to Δz as

$$\Delta I(\mathbf{R}_\parallel, z_0) + \frac{\partial I}{\partial z}(\mathbf{R}_\parallel, z_0)\Delta z = 0. \tag{2.24}$$

This relation can be rewritten as

$$\Delta z = -\Delta[\log I(\mathbf{R}_\parallel, z_0)] \times \frac{I(\mathbf{R}_\parallel, z_0)}{\frac{\partial I}{\partial z}(\mathbf{R}_\parallel, z_0)}. \tag{2.25}$$

With this relation, the change of the current can be converted to the change of the tip height. We can accurately calculate the change of the current, but use an approximation for the proportional coefficient, $I/\frac{\partial I}{\partial z}$. The current is represented by summation of $(\mathbf{k}_\parallel, \mathbf{G}_\parallel)$ elements, and each element decays exponentially with increase of the tip height into the vacuum, because the surface wave function decays exponentially. In the region far enough from the surface, the main contribution to the current comes from the element of $(\mathbf{k}_\parallel = \vec{0}, \mathbf{G}_\parallel = \vec{0})$ because this element decays most slowly. Therefore the dependence of the tunneling current on the tip position is approximately exponential and the proportional coefficient in eq.(2.25) is approximately given by the decay constant of the element of $(\mathbf{k}_\parallel = \vec{0}, \mathbf{G}_\parallel = \vec{0})$. Then eq.(2.25) can be rewritten as

$$\Delta z = \frac{1}{2\sqrt{2m\phi_0/\hbar^2}}\Delta[\log I(\mathbf{R}_\parallel, z_0)]. \tag{2.26}$$

Thus logarithm of the current distribution at the same tip height would correspond to the approximate corrugation image with constant current. In this article, all STM/STS mapping images are calculated from this approximation. The maps of the LDOS distribution in this article also follow this approximation.

As for the STS spectrum, the ordinary experimental spectrum is calculated from $(dI/dv)/(I/v)$ so as to be normalized to 1 at $v = 0$ to avoid complication by the difference of absolute value of the tunneling current. We use often this 'normalized' STS spectrum also in this article.

Chapter 3

Case Study of Si(001) Reconstructed Surfaces

§1. Simulation of Si(001) Reconstructed Surfaces

In this chapter, we show the results of the theoretical simulation of STM/STS by our method which is applied to Si(001) reconstructed surface as a case study. Hereafter, we refer our method as "connected vacuum tails (CVT) method", and the method directly calculating the tails from LCAO wave functions without connecting the wave functions as "ordinary LCAO method". For this surface, the STM/STS observation plays an important role to analyze the structure of the reconstruction as mentioned before. Thus the theoretical simulation of STM/STS will also contribute to our understanding on the Si(001) surface. At the same time, we will be able to examine the validity of CVT method, and perform the comparison between the present CVT method and the ordinary LCAO method.

In this surface, many types of reconstructions have been reported, but here we discuss only the (2×1) symmetric dimer structure, and the c(4×2) asymmetric dimer structure. First we will show the result of the cluster calculation of the W_{10} (111) tip by the DV-Xα-LCAO-cluster method and give some comments on the character of the electronic states. Next we show the results of simulation for the (2×1) symmetric dimer structure, and the c(4×2) structure. And, we also discuss the validity of our method.

§2. Character of the Model Tip
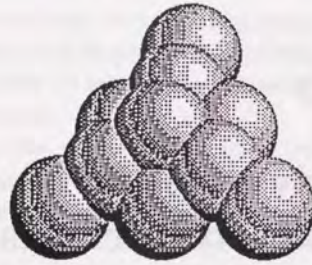
Figure 3.1: The structure of the model tip cluster W_{10}. The tip is cut from the bulk crystal and the direction of the axis is [111].

We model the tip as a W_{10} cluster cut from bulk crystal, whose axis is directed toward [111]. As seen in the tip structure shown in Fig.3.1, there is a C_3 symmetry axis parallel to [111] direction. And we introduce the width, $\Delta = 1.0$eV to each level. This width is evaluated according to the width of the d-band peak of bulk tungsten [106]. This model of the tip was used by Isshiki *et al.* [62].

The electronic structure was calculated with the DV-Xα-LCAO cluster method, as was done in the work by Isshiki *et al.* The levels near the Fermi energy are made from $6s$ and $5d$ orbitals. Table 3.1 shows the LCAO coefficients of the tip top AO's around the HOMO level. The levels around the HOMO are made not only from $6s$ or $5d_{z^2}$ AO's but also $5d_{x^2-y^2}$, or $5d_{xy}$, $5d_{xz}$, $5d_{yz}$.

Fig.3.2 shows the DOS of this tip with the width 1.0eV. The summation of the levels is cut at $E_F \pm 4.0$eV in this DOS calculation. The figure shows an almost flat DOS spectrum around the Fermi energy. If the tunneling current is equally contributed by all the tip levels, the STS spectrum would reflect the surface LDOS, though we cannot neglect the contribution from the second term of the right hand side of eq.(1.16).

But as a result of decay of the surface wave functions, the tip top orbitals would mostly contribute to the tunneling current. Isshiki *et al.* reported that the STM tunneling current flows mainly through the tip top AO's, and the contribution from other AO's is only several %. The calculation of the transfer matrix elements needs a large computational time, because there are a large number of combinations of

Table 3.1: The LCAO coefficients of the tip top atom's AO's are presented. The levels around the HOMO are chosen.

Energy [eV]	$6s$	$5d_{x^2-y^2}$	$5d_{xy}$	$5d_{xz}$	$5d_{yz}$	$5d_{zz}$	
−3.98	0.0	−0.073	0.042	−0.232	−0.134	0.000	
−3.98	0.0	0.042	0.073	0.134	−0.232	0.000	
−3.87	0.0	0.077	−0.044	0.026	0.015	−0.000	
−3.87	0.0	−0.044	−0.077	−0.015	0.026	0.000	
−3.64	−0.025	−0.000	0.0	0.0	0.0	−0.073	
−3.58	0.0	0.0	0.0	0.0	0.0	0.0	
−3.45	−0.114	0.000	0.0	−0.000	0.0	−0.051	
−3.09	0.0	0.245	−0.141	−0.103	−0.060	−0.000	
−3.09	0.0	−0.141	−0.245	0.060	−0.103	−0.000	
−3.00	0.0	−0.171	0.099	−0.254	−0.147	0.000	
−3.00	0.0	0.099	0.171	0.147	−0.254	0.000	
−2.72	0.008	0.000	0.0	0.0	0.0	−0.165	
−2.69	0.0	0.0	0.0	0.0	0.0	0.0	
−2.51	0.0	0.085	−0.049	0.143	0.083	0.000	
−2.51	0.0	−0.049	−0.085	−0.083	0.143	−0.000	
−2.43	0.017	0.0	0.0	0.0	0.0	0.093	
−2.38	0.0	−0.173	0.100	−0.061	−0.035	0.000	HOMO
−2.38	0.0	0.100	0.173	0.035	−0.061	0.000	HOMO
−2.35	0.0	0.0	0.0	0.0	0.0	0.0	LUMO
−2.32	0.0	−0.131	0.076	−0.046	−0.027	0.000	
−2.32	0.0	0.076	0.131	0.027	−0.046	0.000	
−2.30	0.0	0.230	−0.133	0.112	0.065	0.0	
−2.30	0.0	−0.133	−0.230	−0.065	0.112	−0.000	
−2.27	−0.011	−0.000	0.0	0.0	0.0	0.064	
−2.19	0.0	−0.105	0.061	−0.121	−0.070	0.0	
−2.19	0.0	0.061	0.105	0.070	−0.121	0.000	
−1.99	−0.068	0.0	0.0	0.000	−0.000	−0.313	
−1.90	0.0	−0.226	0.130	0.327	0.189	−0.000	
−1.90	0.0	0.130	0.226	−0.189	0.327	−0.000	
−1.47	0.011	0.000	0.0	−0.000	−0.000	−0.420	
−1.41	0.0	0.0	0.0	0.0	0.0	0.0	
−1.12	0.0	−0.153	0.089	−0.201	−0.116	0.000	
−1.12	0.0	0.089	0.153	0.116	−0.201	0.000	
−1.00	0.0	−0.105	0.061	0.425	0.245	−0.000	
−1.00	0.0	0.061	0.105	−0.245	0.425	−0.000	
−0.98	−0.177	0.0	0.0	0.000	0.0	0.619	
−0.65	0.0	−0.094	0.054	0.140	0.081	0.000	
−0.65	0.0	0.054	0.094	−0.081	0.140	−0.000	
−0.45	0.016	0.0	0.0	−0.000	0.000	0.265	
−0.39	0.0	0.297	−0.171	−0.246	−0.142	0.000	
−0.39	0.0	−0.171	−0.297	0.142	−0.246	−0.000	
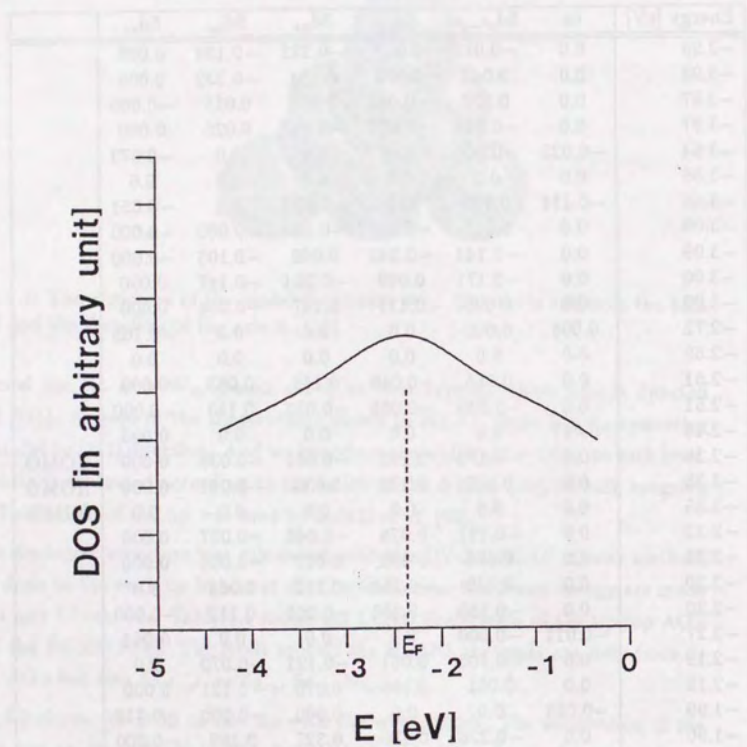
Figure 3.2: The DOS spectrum near Fermi surface of the tip cluster. All the width of levels, Δ, are 1.0eV.
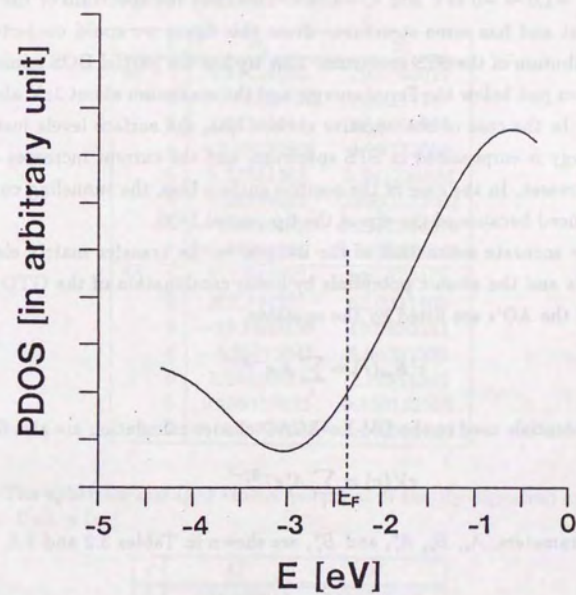
Figure 3.3: The partial DOS spectrum at the tip top atom is presented. The partial DOS is calculated by Mulliken charge analysis.

the AO's, the atom potentials and the plane waves. In the following calculation, therefore, the tunneling matrix elements are calculated taking into account only the tip top AO's and the tip top atomic potential, and the effects of other AO's and atomic potentials are neglected.

Fig.3.3 shows the partial DOS of the tip top atom obtained from the Mulliken charge analysis. The levels which have much contribution to the tip top partial DOS are located at $-1.0 \sim -0.4$eV and < -4.8eV. Therefore the spectrum of the partial DOS is not flat and has some structure. From this figure we could conjecture the intensity distribution of the STS spectrum. This tip has the partial DOS minimum of the tip top atom just below the Fermi energy, and the maximum about 1eV above the Fermi energy. In the case of the negative surface bias, the surface levels just below the Fermi energy is emphasized in STS spectrum, and the current increases quickly as the bias increases. In the case of the positive surface bias, the tunneling current is somewhat reduced because of the dip of the tip partial DOS.

For a more accurate estimation of the integral in the transfer matrix elements, we fit the AO's and the atomic potentials by linear combination of the GTO's. The radial parts of the AO's are fitted by the equation,

$$r^l R_{nl}(r) = \sum_i A_i e^{-B_i r^2}. \tag{3.1}$$

The atomic potentials used in the DV-Xα-LCAO-cluster calculation are also fitted as

$$rV(r) = \sum_i A_i^v e^{-B_i^v r^2}. \tag{3.2}$$

The fitting parameters, A_i, B_i, A_i^v, and B_i^v, are shown in Tables 3.2 and 3.3.

§3. Simulation of Si(001) (2×1) Symmetric Dimer Surface

§3.1 Results of Band Calculation

We calculate the electronic structure of the surface, Si(001) (2×1) symmetric dimer surface, by the DV-Xα-LCAO band method with the isolated slab model. The used geometry is Levine's model [107], in which only the first layer atoms of the surface are reconstructed and form symmetric dimers with the same bond length as in the bulk. The slab has eight layers of silicon and one layer of hydrogen, which terminates the dangling bonds of Si at the opposite side of the slab. The unit cell has sixteen Si

Table 3.2: The radial part of the numerical basis, i.e. atomic orbitals, on the tip top atom are fitted by Gaussian's. Unit is [au].

	i	A_i	B_i
6s	1	9.81624603	2007.80029
	2	−5.89828777	101.131317
	3	4.96218491	22.0662994
	4	−2.89008808	4.29772568
	5	1.32351303	0.742234886
	6	7.56019402	0.0993523002
	7	−13.5240002	0.0907154679
	8	5.64599991	0.0830867290
5d	1	811.041992	225.878479
	2	272.134277	62.0221405
	3	−19.1830139	10.5890551
	4	−6.86813641	5.66381359
	5	1.09816837	1.14854240
	6	0.299157023	0.438152909
	7	0.0347734541	0.142964005

Table 3.3: The spherical averaged atomic potential of the tip top atom are fitted by Gaussian's. Unit is [au].

i	A_i^v	B_i^v
1	−4.70308018	11577.5703
2	−11.6188002	573.668457
3	−20.3193054	57.7987823
4	−23.9593658	7.51026917
5	−10.9979982	0.994826972
6	−2.08028412	0.0550469682
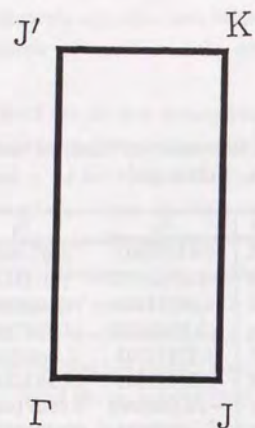
Figure 3.4: The shape of the first Brillouin zone of the (2×1) Structure.

atoms and eight H atoms. Fig.1.4 is a reference for the shape of the unit cell. The Brillouin zone is shown in Fig.3.4.

The calculated band dispersion relation is shown in Fig.3.5. In the bulk band gap, there are two surface bands, and they both have a significant dispersion in the y direction but only a weak dispersion in the x direction, i.e. they are 1D like bands along the dimer row. This surface is metallic, and the Fermi surface goes across these two bands. Their band widths are about 0.8eV, and they have small peaks along J-K line, and J′-Γ line. These characters are essentially the same as those which have been reported up to now.

Fig.3.6 is the DOS spectrum near the surface band. One peak is found in lower edge, two peaks are in upper edge, and two peaks are in the center. Roughly speaking, the DOS looks like a sum of two 1D-like cosine band DOS, consistent with the dispersion relation.

In our calculation, the bulk band gap is too wide, ~ 3eV. This is due to the band method used for the calculation. The isolated slab model reduces the bulk band width, and enhances the width of the bulk band gap. In addition, the minus of Fermi energy of our calculation, 2.32eV, is too small compared with the work function, 4.8eV of Si. The small value of the work function is partly due to the LCAO approximation
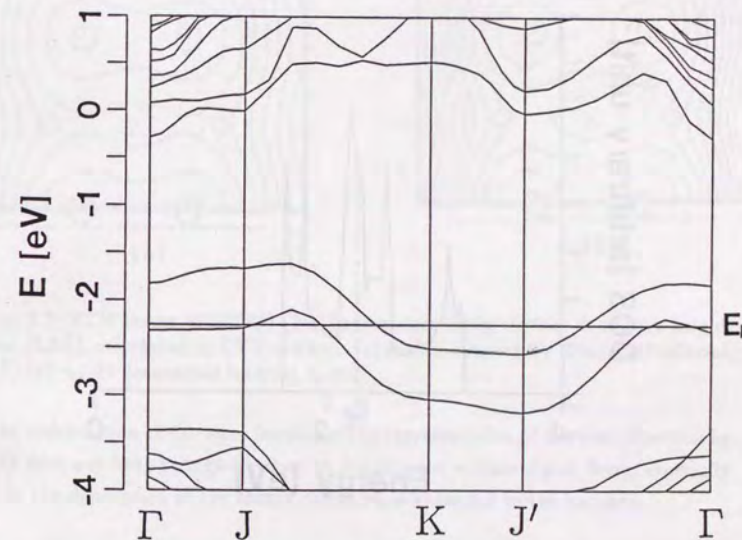
Figure 3.5: The calculated band dispersion relation of Si(001) (2×1) symmetric dimer is presented. The two bands near the Fermi energy are surface bands.
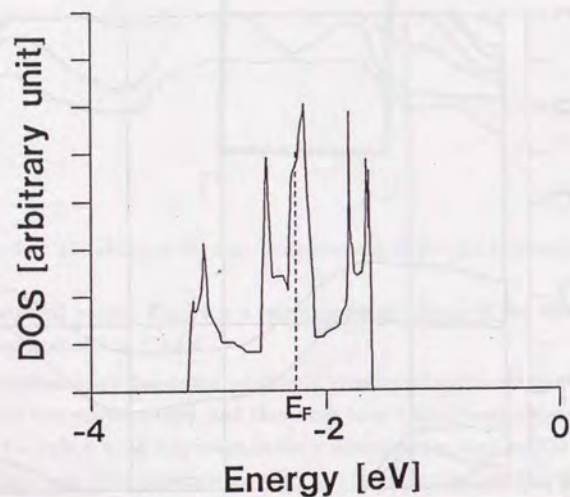
Figure 3.6: The calculated DOS spectrum of the Si(001) (2×1) symmetric dimer structure around the band gap.
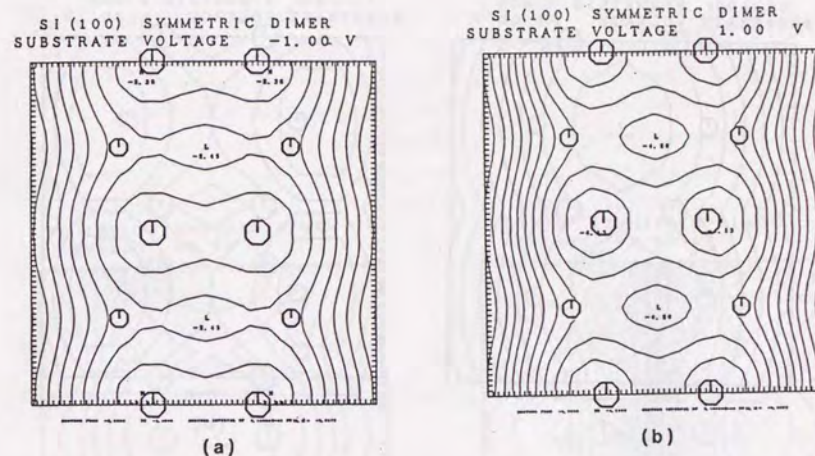
Figure 3.7: STM image of Si(001) (2×1) symmetric dimer surface at the tip height, 10.0au (5.3Å), calculated by CVT method. (a) surface bias −1.0V [converted interval, 0.03Å] (b) +1.0V [converted interval, 0.04Å]

for the construction of the wave function. The representation of the wave function by LCAO does not have enough freedom to describe the surface dipole layer, especially poor in the description of the charge distribution extended to the vacuum.

§3.2   Simulated Results of STM

Fig.3.7 shows the simulated STM images at the tip height 10.0au (5.3Å). The octahedrons represent the outer two layer atoms of the surface. This tip position is the boundary between the intermediate and the vacuum region described in Chapter 2. Because the wave functions in the intermediate region behave as almost free waves in the neighbor of this position, our method would be valid here.

We choose the experimental work function as the tunneling barrier height, 4.8eV, and the positions of the surface-intermediate boundary and the vacuum-intermediate boundary as 2.0au (1.1Å) and 10.0au (5.3Å) respectively from the outermost surface atom. The reciprocal vector cut-off's used in the calculation are taken as $|G_{c1}|^2 =$

SI (100) SYMMETRIC DIMER
SUBSTRATE VOLTAGE   −1. 00 V

SI (100) SYMMETRIC DIMER
SUBSTRATE VOLTAGE   1. 00   V

(a)

(b)
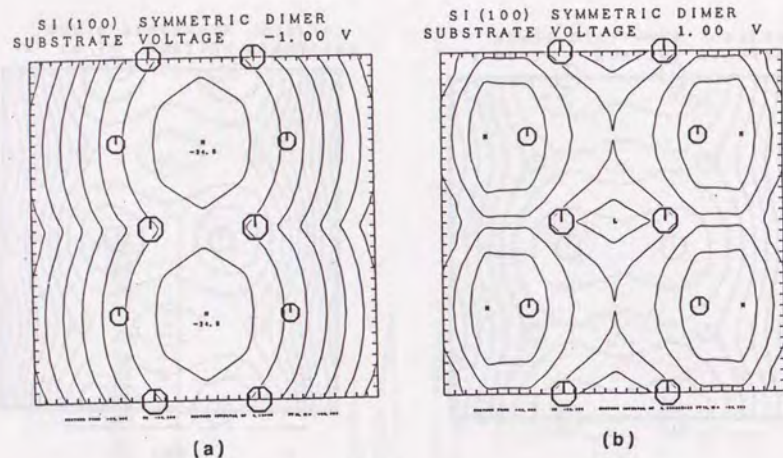
Figure 3.8: STM image of Si(001) (2×1) symmetric dimer surface at the tip height, 20.0au (10.6Å), calculated by CVT method. (a) surface bias −1.0V [converted interval, 0.01Å] (b) +1.0V [converted interval, 0.05Å]

9.0Ry and $|G_{c2}|^2 = 2.25$Ry. In this article, we use these values for parameters of the calculation except for the cases specially indicated. Comments on the choice of these values will be described in other section.

Though the shape of the current contour map for the surface bias +1.0V (Fig.3.7(b)) has a little trace of the nodal structure across the dimer bridges, both images of Fig.3.7(a) and (b) have almost the same bean-like shape. The simulated STM image for the negative surface bias represents fairly well the experimental observation. However, the simulated image for the positive surface bias does not reproduce the observed nodal structure running through the middle of each dimer row. Moreover, when the tip height is 20au (10.6Å), the calculated STM images have the peaks not above the bridge but among the bridge. (see Fig.3.8)

To investigate the reason for the disappearance of the nodal structure, first we calculate the logarithm maps of the surface LDOS distribution at this height. The results for $E = -2.63$eV $(E = E_F - 0.31$eV$)$ and -2.01eV $(E = E_F + 0.31$eV$)$ are

SI (100) SYMMETRIC DIMER
ENERGY −2. 63 eV

SI (100) SYMMETRIC DIMER
ENERGY −2. 01 eV

(a)

(b)
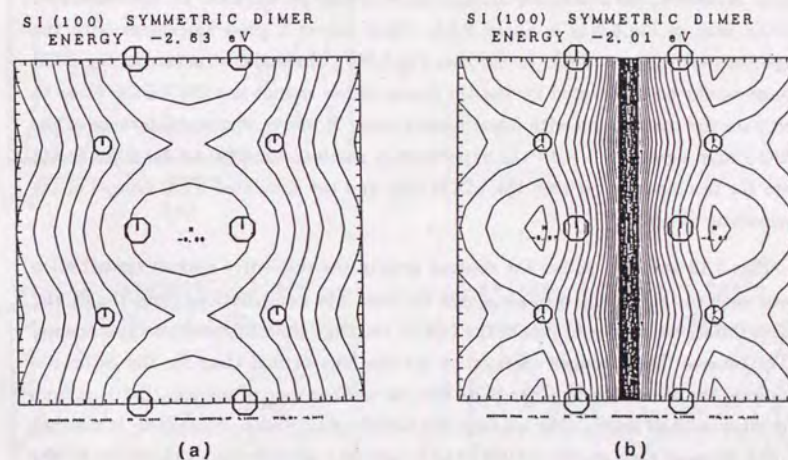
Figure 3.9: Logarithmic distribution maps of LDOS of the Si(001) (2×1) symmetric dimer surface at the tip height of 10.0au (5.3Å) calculated by the CVT method. (a) lower surface band (−2.63eV) [converted interval, 0.07Å] (b) upper surface band (−2.01eV) [converted interval, 0.08Å]

shown in Fig.3.9 (a) and (b) respectively. In the lower surface band, as seen in Fig.3.9 (a), the LDOS is concentrated on the bridge region of the dimer. This reflects the fact that the lower surface band is the bonding state of the dimer dangling bonds. In the upper surface band, as seen in Fig.3.9 (b), the LDOS has a node across the dimer bridge. This reflects the feature of the upper surface band, which is the anti-bonding state of the dangling bonds. These figures reproduce some feature of the experimental STM images; the occupied state shows bean-like shape, while the valley across the bridge is deeper than that between the dimer rows for the unoccupied state. Moreover, the maximum corrugation estimated by eq.(2.26) for the calculated LDOS map of Fig.3.9(a) is about 0.6Å, which shows a good agreement with the experimental value, $\sim$ 0.8Å. In the case Fig.3.9(b), the nodal structure of the STM image would be moderated by the tip states, so we cannot use the LDOS value to compare the corrugation with experimental data. However, the nodal feature of the LDOS map agrees well with the experimental results. Anyhow we have confirmed here the discrepancy between the LDOS map and the simulated STM images of the symmetric dimer.

Figs.3.10 and 3.11 shows the contour map of the respective current contribution from each of the atomic orbitals at the tip top. The contributions from the 6s and $5d_{z^2}$ orbitals are similar to that of the LDOS, and they almost reproduce experimental STM image. The stronger corrugation for the $5d_{z^2}$ orbital than for the 6s orbital confirms the discussion by Chen [60]. But the contour map of the contributions from the other orbitals are far different from the LDOS contour map. The reason is ascribed to the shape of each atomic orbital. The 6s and $5d_{z^2}$ orbitals have s character for the rotation around the z-axis of the tip. Thus the character of the LDOS contour map is reflected on the simulated images. The $5d_{xz}$ and $5d_{yz}$ orbitals have p character, and the $5d_{x^2-y^2}$ and $5d_{xy}$ orbitals have d character around the z-axis of the tip. Thus, the peaks and the nodes are moved from original positions in images by these atomic orbitals. Especially, the $5d_{xz}$ orbital and $5d_{xy}$ orbital move away the original node. Our model tip has many levels, constructed by the $5d_{xz}$, $5d_{yz}$, $5d_{x^2-y^2}$, and $5d_{xy}$ orbitals, around the Fermi energy. All contributions from those levels except 6s and $5d_{z^2}$ reduce the corrugation of the image obtained from the 6s and $5d_{z^2}$ orbitals. It seems that this is one of the reason why our simulated images do not correspond to the LDOS images.

For the negative surface bias, as seen in Fig.3.10, the corrugation in the simulated image is about 0.2Å and that obtained only with the 6s or $5d_{z^2}$ orbitals is about 0.3Å

(a)

(b)   (c)
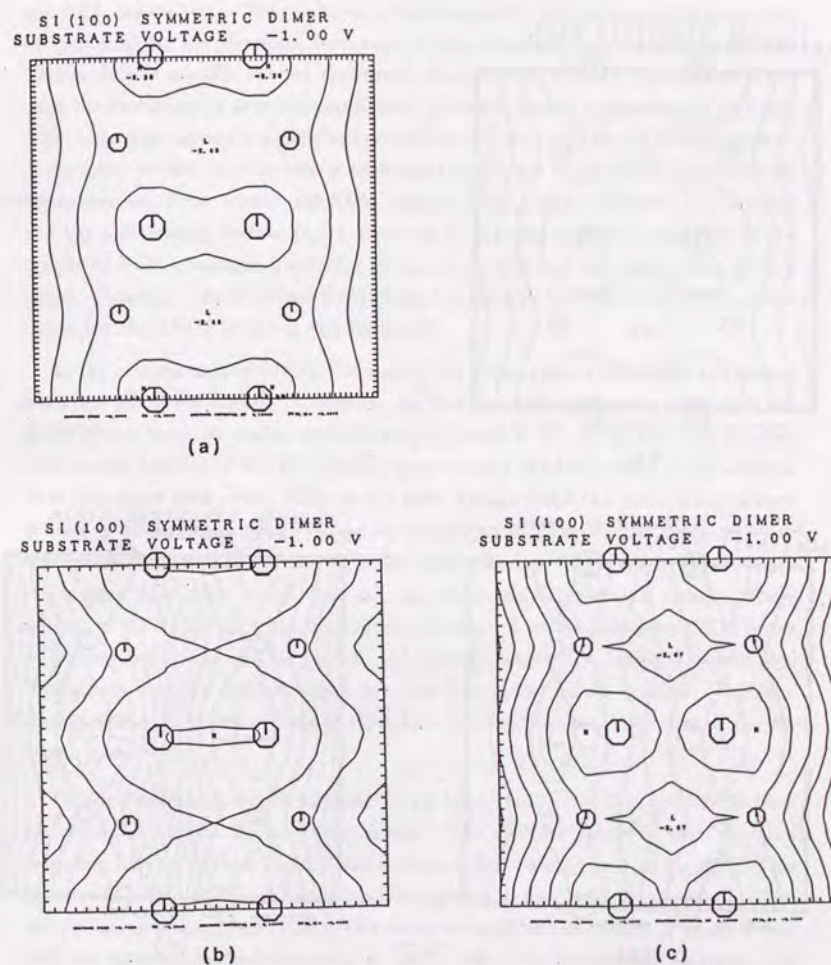
Figure 3.10: The contribution from the tip top AO's to the STM image of Si(001) (2×1) symmetric dimer surface at the tip height, 10.0au (5.3Å), calculated by CVT method. The surface bias is −1.0eV and converted interval is 0.06Å. (a) total, (b) from 6s orbital, (c) from $5d_{z^2}$.

SI (100) SYMMETRIC DIMER
SUBSTRATE VOLTAGE   1.00 V

(a)

SI (100) SYMMETRIC DIMER
SUBSTRATE VOLTAGE   1.00 V

SI (100) SYMMETRIC DIMER
SUBSTRATE VOLTAGE   1.00 V

(b)

(c)
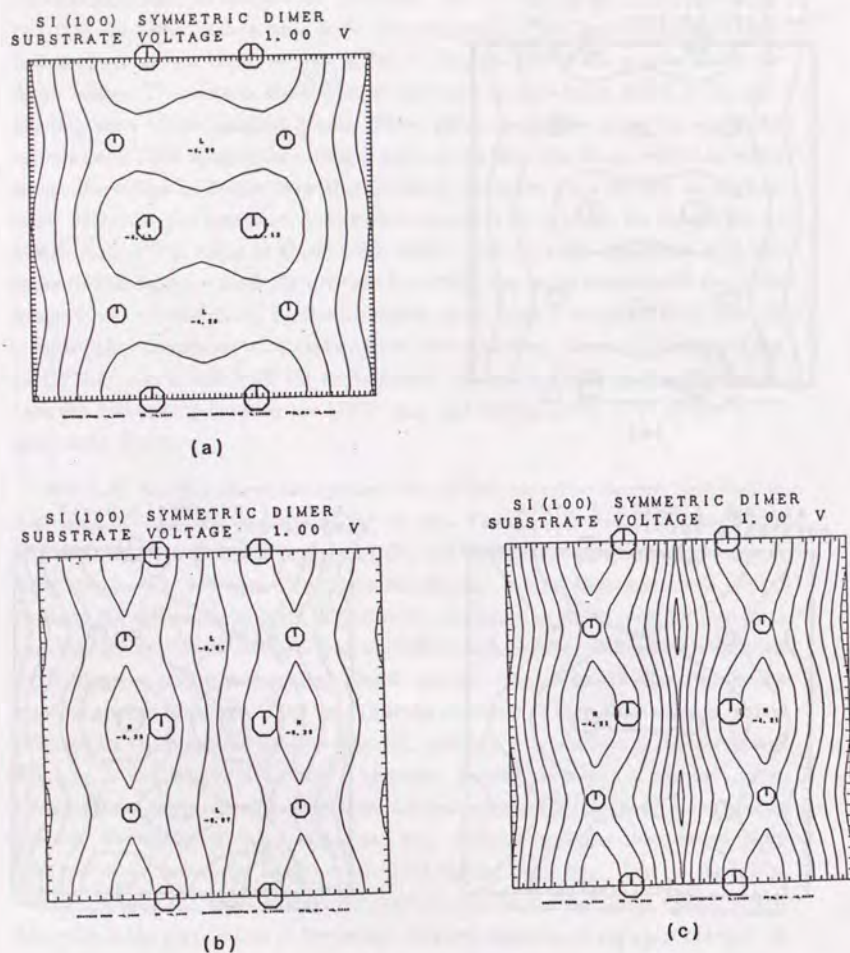
Figure 3.11: The contribution from the tip top AO's to the STM image of Si(001) (2×1) symmetric dimer surface at the tip height, 10.0au (5.3Å), calculated by CVT method. The surface bias is 1.0eV and converted interval is 0.09Å. (a) total, (b) from 6s orbital, (c) from $5d_{z^2}$.

whereas the experimental corrugation and that estimated by the LDOS are about 0.8Å and 0.6Å, respectively. The smallness of the corrugation for the simulated image can be explained by the electronic structure of the symmetric dimer model as follows. This surface is metallic for the symmetric dimer model and the two surface bands cross the Fermi energy as mentioned before. For both cases of surface bias of +1V and −1V, tunneling current is significantly contributed from the peak of LDOS originated in the lower surface band as well as that originated in the upper band. Therefore, for the symmetric dimer model, the STM image is contributed both from the bonding and the antibonding surface states, resulting in the reduction of corrugation in the simulated STM images, in particular the nodal structure of the antibonding surface states. Therefore, the simulated STM image corresponds to neither the experimental image nor the LDOS image at this tip height.

In the contour map of LDOS, the node of the upper surface band does not change when the tip moves higher. In addition, we find that the corrugation parallel to the dimer bridge becomes weaker and that perpendicular to the bridge becomes stronger with higher position of the tip. In the upper surface band the peaks move outward as if they repel each other, while in the lower surface band the peaks move inward as if they attract each other. When the tip moves still higher, the peaks move to the intermediate site of bridges for both surface bands. Thus, at tip height much larger than 10au, the LDOS does not reproduce the experimental image. These aspects of the LDOS far from the surface are reflected on the calculated STM image as exemplified in the case of Fig.3.8. At this tip height, the image is contributed dominantly from d_{z^2} orbital, which does not deform the LDOS contour. Therefore the simulated STM image cannot reproduce the experimental one, even if the tip height is moved.

On the other hand, we can evaluate the tip height realized in the experiments from the absolute value of the tunneling current. The absolute values of the calculated tunneling current for the surface bias voltage of ±1V are plotted in Fig.3.12. This figure reveals that the tunneling current changes about one order of magnitude, when the tip moves about 2.5au (1.3Å). The decay constant of the current is about 0.9au, and this value approximately equals $2\sqrt{\frac{2m}{\hbar^2}E_w}$, where E_w is the work function, now assumed to be 4.8eV. This is a natural result of our method, and the same as the simple 1D WKB tunneling theory. In the experiment of STM, the typical value of the current is 1nA for the bias, 1V. Then, based on Fig.3.12, the tip position is estimated to be located at about 22au (12Å) from the outermost atom. If we take into
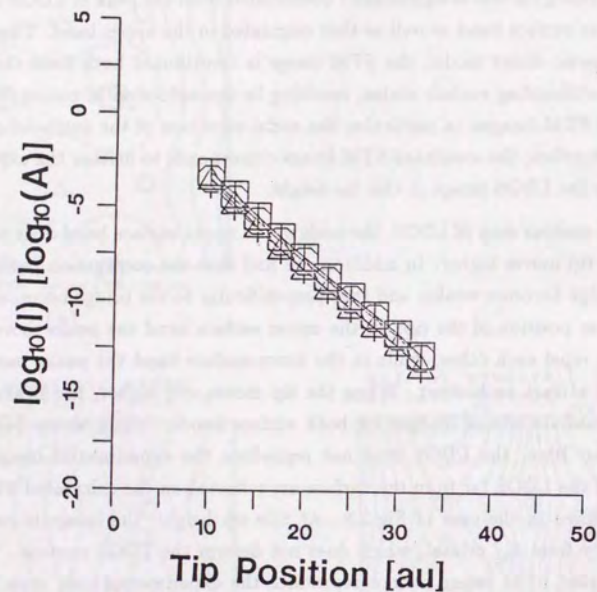
Figure 3.12: The relation between tunneling current and tip position in case of Si(001) (2×1) symmetric dimer surface, calculated by CVT method.
□ — maximum current at surface bias −1.0V.
○ — minimum current at −1.0V.
△ — maximum current at +1.0V.
+ — minimum current at +1.0V.
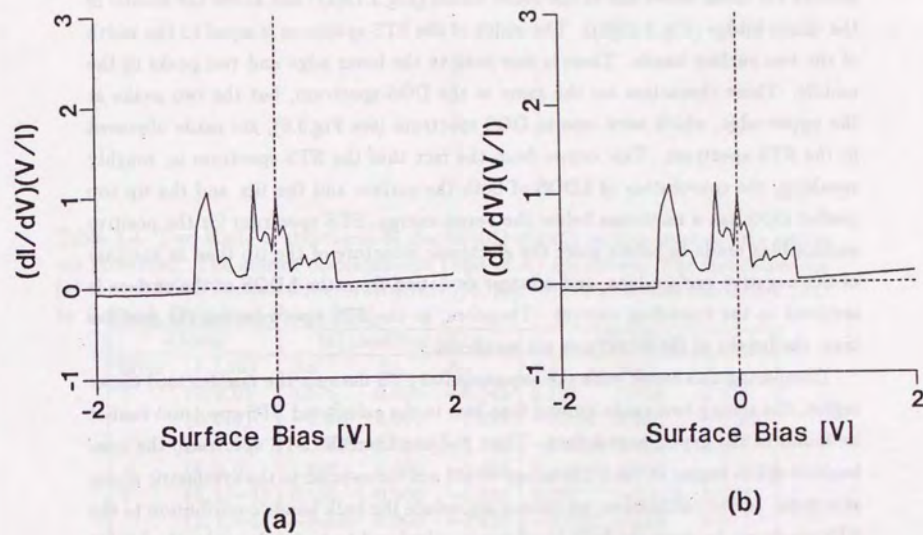
Figure 3.13: Normalized STS spectrum of Si(001) (2×1) symmetric dimer at the tip height, 10.0au (5.3Å), calculated by CVT method. (a) above one of the dimer atoms (b) above middle of the dimer bridge.

account the image potential which reduces the barrier effect, this tip height should be estimated still larger.

This value of the tip height is somewhat larger than that inferred by Bono and Good [41], which is about 8Å, though the situation is different between theirs and ours. They treated the STM tunneling as M-I-M junction, and calculated the tunneling current by 1D WKB tunneling theory considering the effect of the image potential. It seems possible to calculate the absolute value of the STM tunneling current with reasonable accuracy using our method.

§3.3   Simulated Results of STS

Fig.3.13 shows the normalized STS spectra at the tip height, 10.0au (5.3Å). The STS spectra are taken above one of the dimer atoms (Fig.3.13(a)) and above the middle of the dimer bridge (Fig.3.13(b)). The width of the STS spectrum is equal to the width of the two surface bands. There is one peak in the lower edge and two peaks in the middle. These characters are the same as the DOS spectrum, but the two peaks at the upper edge, which were seen in DOS spectrum (see Fig.3.6), are made obscured in the STS spectrum. This comes from the fact that the STS spectrum is, roughly speaking, the convolution of LDOS of both the surface and the tip, and the tip top partial DOS has a minimum below the Fermi energy. STS spectrum for the positive surface bias tends to reflect more the electronic structure of the tip than in the case of the negative surface bias, and a larger deviation from the LDOS of the surface is involved in the tunneling current. Therefore, in the STS spectrum for the positive bias, the height of the structures are weakened.

Comparing this result with the experimental STS data on the non-buckled dimer region, the strong two peaks around zero bias in the calculated STS spectrum cannot be found in the experimental data. Thus, judging from the STS spectrum, the non-buckled dimer region in the STM image would not correspond to the symmetric dimer structure. In our calculation, we cannot reproduce the bulk bands contribution to the STS spectrum because the bulk band gap is calculated to be too large by the LCAO method for the isolated slab model.

Returning to the calculated STS spectra, the STS spectra do not change so much for both sites above one of the dimer atom and above middle of the bridge. If the STS reflects directly the surface LDOS, the unnormalized STS spectrum above the middle of the bridge should be terminated in the positive surface bias, but this is not the case in the calculated results. This is due to the character of the tip allowing the tunneling current contribution from the $5d_{x^2-y^2}$, $5d_{xy}$, $5d_{xz}$, and $5d_{yz}$ orbitals. Because of the non-axial symmetry of these orbitals, the STS cannot be determined by the purely local information of the surface electronic states at the tip top position, but affected by the electronic states at nearby regions. This feature arises from the terms with higher order terms of the differential of Green's function as in eq.(1.16), and also verified by a similar argument as the one by Chen [60].

§4. Simulation of Si(001) c(4×2) Surface

§4.1 Results of Band Calculation

Table 3.4: Two kinds of structures of the Si(001) c(4×2) surface used in this article are presented. The atomic displacements (unit of Å) are shown. The structures are (a) the modified Yin and Cohen's structure [83, 93], (b) the structure based on LEED by Holland, Duke, and Paton [108].

Atoms		(a) modified YC's			(b) HDP		
layer	(k,l,m)	Δx	Δy	Δz	Δx	Δy	Δz
1	$(0,0,0)$	0.578	0.000	−0.149	0.593	0.000	0.170
	$(2,0,0)$	−1.048	0.000	−0.498	−0.954	0.000	−0.460
	$(6,0,0)$	−0.578	0.000	−0.149	−0.593	0.000	0.170
	$(4,0,0)$	1.048	0.000	−0.498	0.954	0.000	−0.460
2	$(0,1,-1)$	0.115	0.000	−0.010	0.092	−0.113	0.071
	$(2,1,-1)$	−0.115	0.000	−0.010	−0.092	0.113	0.071
	$(4,1,-1)$	0.115	0.000	−0.010	0.092	0.113	0.071
	$(6,1,-1)$	−0.115	0.000	−0.010	−0.092	−0.113	0.071
3	$(1,1,-2)$	0.000	0.000	−0.225	0.000	0.000	−0.057
	$(3,1,-2)$	0.000	0.000	0.124	0.000	0.004	0.166
	$(5,1,-2)$	0.000	0.000	−0.225	0.000	0.000	−0.057
	$(7,1,-2)$	0.000	0.000	0.124	0.000	−0.004	0.166
4	$(1,2,-3)$	0.000	0.000	−0.180	−0.033	0.000	−0.029
	$(3,2,-3)$	0.000	0.000	0.085	0.000	0.000	0.127
	$(5,2,-3)$	0.000	0.000	−0.180	0.033	0.000	−0.029
	$(7,2,-3)$	0.000	0.000	0.085	0.000	0.000	0.137
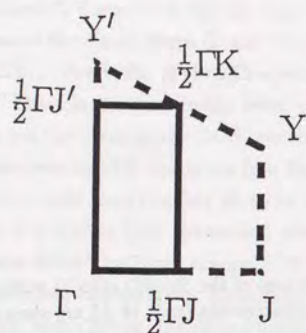
Figure 3.14: The shape of the first Brillouin zone of the c(4×2) structure (broken line) and the folded Brillouin zone for the surface unit cell used in our calculation (solid line).

In this section, we show the calculated results of the electronic structure of Si(001) c(4×2) surface. The used geometry is obtained by a slight modification of Yin and Cohen's structure [83, 93], in which the unit cell of (2×1) asymmetric dimers are arranged to make c(4×2) structure (Table 3.4 (a)). The surface primitive cell of the c(4×2) structure is rhombic, but in order to use the same program as for the symmetric dimer, we use the rectangular surface unit cell, which is two times larger than the primitive cell and has a similar shape as that of (2×1) unit cell. (see Fig.1.4 (c)) The slab has four layers of silicon and one layer of hydrogen, which terminates the dangling bonds of silicon at the opposite side of the slab. The unit cell includes 32 Si atoms and 16 H atoms. The Brillouin zone for the c(4×2) structure is shown in Fig.3.14.

The calculated band dispersion relation is shown in Fig.3.15. In the bulk band gap, there are eight surface bands. This surface is semiconducting, and the surface band gap is indirect, the gap energy being 0.45eV. The lower four surface bands are occupied and the upper four surface bands are unoccupied. The Fermi energy is chosen to be at the middle of the surface band gap. The character of the surface bands are essentially the same as that of the calculated result by Zhu *et al.* [93], but the gap is larger than their value, 0.01eV. In this calculation, the bulk band gap is again too wide, ~ 3.4eV. The feature of giving wider energy gap has been generally observed in the DV-Xα-LCAO-band calculations.
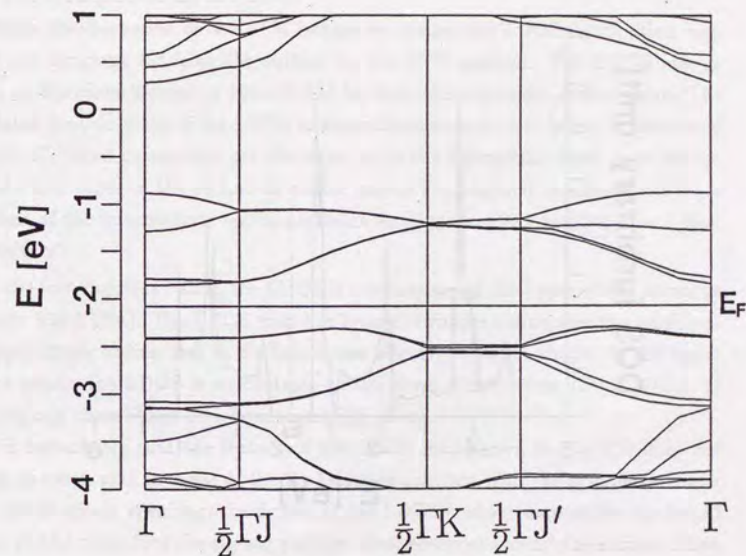
Figure 3.15: The calculated band dispersion relation of Si(001) c(4×2) is presented. The eight bands around the Fermi energy are surface bands.
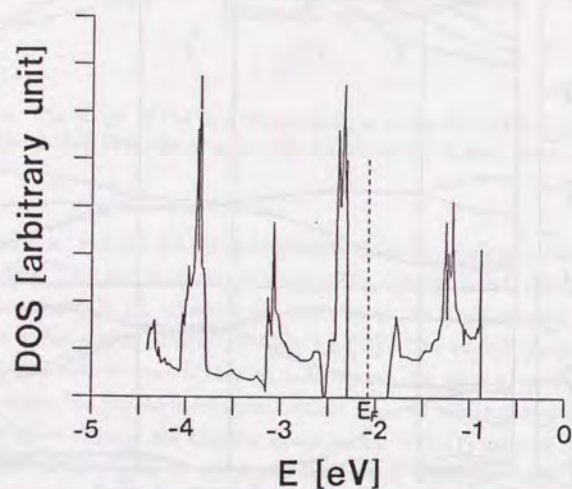
Figure 3.16: The calculated DOS spectrum of the Si(001) c(4×2) structure around the band gap.

Fig.3.16 shows the DOS spectrum in the energy region of the surface bands. The structures in $-3.2 \sim -0.8$eV come from the surface bands. The lower four surface bands seem to make up one 1D cosine like band, and the same is the case for the upper four surface bands. Two peaks are found both in the lower edge and in the upper edge of the lower surface bands, one peak both in the lower edge and in the upper edge of the upper surface band, and two peaks in the middle of the upper surface bands. The two surface bands of (2×1) symmetric dimer structure repel each other and are separated up and down.

Before the discussion of the STM image, we discuss the LDOS distribution map of c(4×2) structure far from the surface by the CVT method. The LDOS map is shown on the plane located at 10au (5.3Å) far from the outermost surface atom. The calculated contour maps of the LDOS in logarithmic scale at that height is illustrated in Fig.3.17. Used parameters are the same as in the symmetric dimer case, except that the two types of the reciprocal vector cut-off's considered in solving the wave functions of the intermediate region are taken as $|G_{c1}|^2 = 4.0$Ry and $|G_{c2}|^2 = 1.0$Ry, respectively.

In the lower surface bands, the LDOS is concentrate on the upper dimer atoms as shown in Fig.3.17(a). The LDOS map has bean-like shapes connecting the neighboring upper dimer atoms, and as a whole shows a honeycomb-like shape. In the upper surface bands, the LDOS is concentrate on the lower dimer atoms (Fig.3.17(b)). It has a zig-zag chain shape or a honeycomb-like shape.

It is remarkable that the feature of the LDOS map shown in Fig.3.17 does not change so much with increase of the tip height in contrast with the symmetric dimer case. Qualitatively speaking, the figures of the LDOS contour map at the tip height 10.0au (5.3Å) reproduce the zig-zag pattern often observed around the surface defect or the step. At this tip height, the obtained maximum corrugations of the constant LDOS surface are about (a) 1.9Å and (b) 2.2Å, while at the tip height of 20.0au (10.6Å), the corrugations are about (a) 0.8Å and (b) 0.5Å.

§4.2   Simulated Results of STM

Fig.3.18 shows the calculated STM image of Si(001) c(4×2) surface at the tip height 10.0au (5.3Å). Our tip reduces the corrugation of the image compared with that of the LDOS map as in the case of the symmetric dimer structure(Fig.3.17). But the calculated image for the negative surface bias case reproduces the experimental feature of the observed zig-zag part. In the negative surface bias case, only the upper
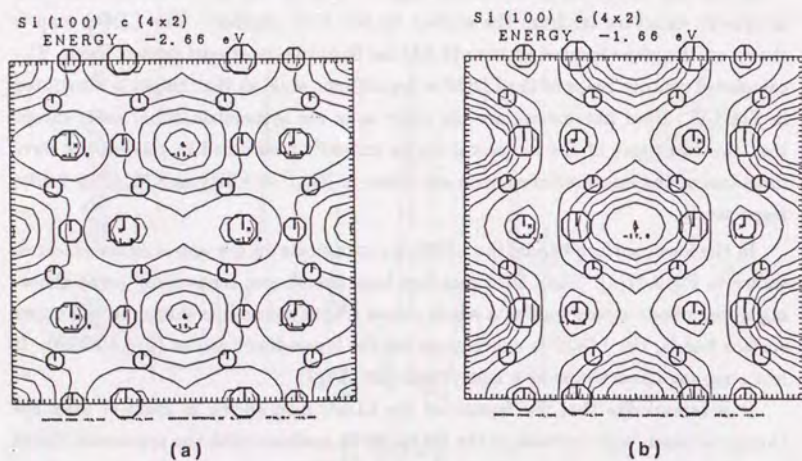
Figure 3.17: Logarithmic distribution maps of LDOS of the Si(001) c(4×2) surface at the tip height of 10.0au (5.3Å) calculated by the CVT method. (a) lower surface band (−2.66eV) [converted interval, 0.3Å] (b) upper surface band (−1.66eV) [converted interval, 0.3Å]
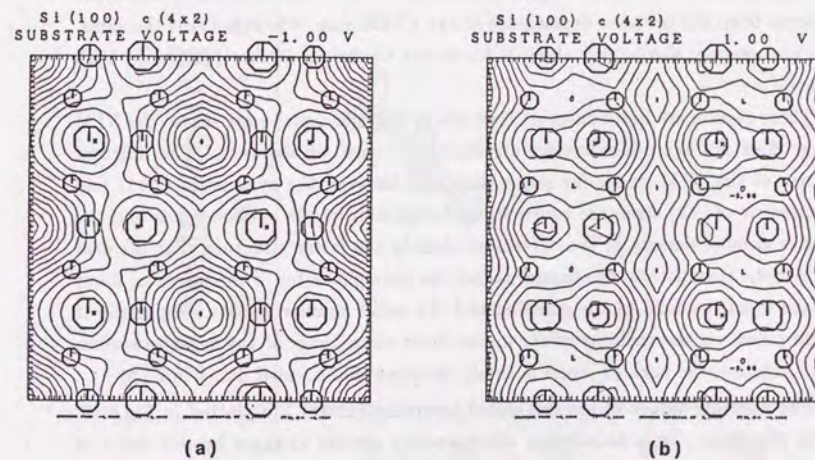
Figure 3.18: STM image of Si(001) c(4×2) symmetric dimer surface at the tip height, 10.0au (5.3Å), calculated by CVT method. (a) surface bias −1.0V [converted interval, 0.06Å] (b) +1.0V [converted interval, 0.09Å]

dimer atom is highlighted, and the image takes a honeycomb-like shape. On the other hand, in the positive surface bias case, the lower dimer atom is highlighted but the upper atom is also highlighted weakly. The maximum corrugations are 0.7Å in both bias.

Even if the tip height increases to larger values ($\gtrsim$20au), the calculated image for the negative surface bias has quite the same honeycomb like image. On the other hand, the calculated STM image for positive surface bias becomes somewhat broader and cannot remind us of the original surface structure. This situation is somewhat different from the distance dependence of the LDOS map, which remains the same. The corrugation also is still about 0.3Å at the tip height 20.0au (10.6Å) in both polarity.

These results are quite different from the symmetric dimer case, where the STM image does not reproduce surface structure for larger tip distance. The different feature of the STM image for larger distances between the symmetric (2×1) and asymmetric c(4×2) structure comes from the splitting of the surface bands and the smaller number density of the outermost atom in the latter structure. For the case of the c(4×2) structure, the images reflect the pure character of the upper or lower surface band, because of the splitting and the small number density. Especially it would reflect on the visibility of the upper dimer atom image at the negative surface bias. Anyhow, the buckled dimer is surely observed as a buckled dimer in STM.

The absolute values of the calculated tunneling current are plotted in Fig.3.19. From this figure, it is found that the tunneling current changes by one order of magnitude when the tip moves about 1.5au (0.8Å). The change of the current is more rapid than in the symmetric dimer case. When the tip is located near the surface, the current flows through both the upper dimer atoms and the lower dimer atoms, but when the tip moves higher, the current flows dominantly through the upper dimer atoms only. The rapid decay of the current would be explained by this effect.

The typical experimental value of the current is 1nA for the bias value, 1V. Then the tip position is about 19au (10Å) from the outermost atom according to Fig.3.19. This value is smaller than that obtained for the symmetric dimer case which is, 22au. This is due to the smaller number density of the outermost layer's atom in this surface.

§4.3 Simulated Results of STS

The STS spectra calculated by CVT method at the tip height of 10.0au (5.3Å) are shown in Fig.3.20. The normalized spectrum cannot be defined in the gap region
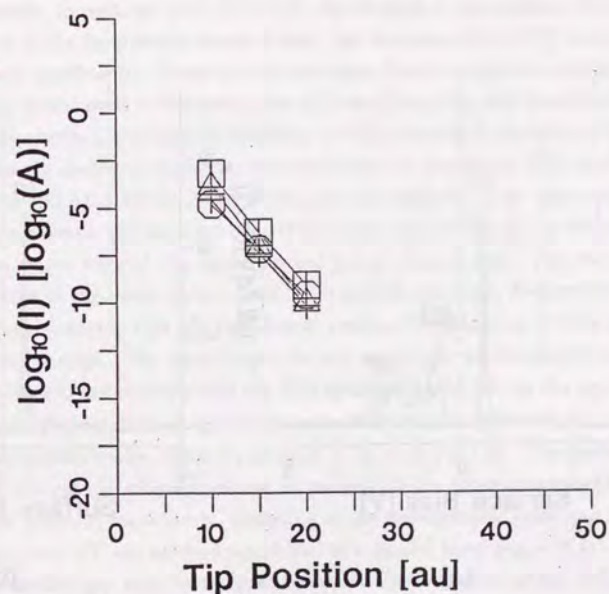
Figure 3.19: The relation between the tunneling current and the tip position in the case of Si(001) c(4×2) surface, calculated by CVT method.
□ — maximum current at surface bias −1.0V.
○ — minimum current at −1.0V.
△ — maximum current at +1.0V.
+ — minimum current at +1.0V.
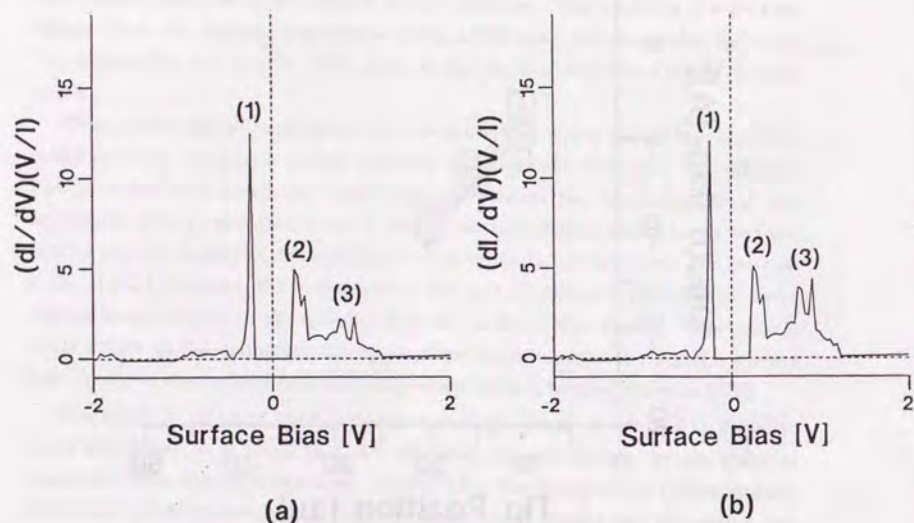
Figure 3.20: Normalized STS spectrum of Si(001) c(4×2) at the tip height, 10.0au (5.3Å), calculated by CVT method. (a) above lower dimer atoms, (b) above upper dimer atom.

where $I = \frac{dI}{dV} = 0$. The STS spectra taken above the lower dimer atom and above the upper dimer atom are shown in Fig.3.20(a) and (b), respectively. On both sites the shapes of the STS spectra are almost similar, as in the symmetric dimer case. It seems that our inclusion of the tip effect makes the structure (3) in the spectrum taken above the upper dimer atom stronger than that in the one taken above the lower dimer atom, in contrast with the LDOS distribution at this height, shown in Fig.3.17. Even if the tip position moves higher, the structure of the STS spectrum does not change significantly. These features are again the same as in the symmetric dimer case. As is discussed in Chapter 1, the STS spectrum does not directly reflect the LDOS of the surface, but, roughly speaking, is determined by a convolution of the surface and the tip electronic structure. The structures are seen in the STS spectrum at (1) $V = -0.3$, (2) $+0.3$, (3) $+0.8$ and $+0.9$V, corresponding to (1) the upper edge of the lower surface bands, (2) the lower edge of the upper surface bands, (3) the saddle point and the upper edge of the upper surface bands, respectively. The structure of the lower edge of the lower surface bands seen in DOS spectrum disappears here, because the strong mixing with the bulk bands weakens the character of the surface state in the lower edge. The peak heights in the upper part of the upper surface bands are weakened, and it seems that the STS spectrum again reflects the tip DOS.

This structure of the STS of c(4×2) structure corresponds well with the experiment on non-buckled image region by Hamers *et al.* (see Fig.1.8). The peaks (1), (2) and (3) in the calculated spectrum can be assigned to the observed peaks labeled with the same numbers respectively. Referring to the experimental band gap in the STS spectrum, ~ 0.7eV, our method would lead to a smaller band gap, ~ 0.4eV. The origin of the smaller gap may be ascribed to several reasons, such as the difference of buckling amplitude, or the strong electron-hole interaction, which is difficult to reproduce by LDA.

§4.4   Dependence on the Buckling Amplitude of Dimer

The result of the angle-resolved ultraviolet photoelectron spectroscopy (ARUPS) measurement for the single domain c(4×2) surface by Kono [98] shows a good coincidence with the theoretical dispersion of the lower surface band calculated by Zhu *et al.* [93] based on the modified Yin-Cohen's structure. Thus we mainly focused the discussions in §4.1∼3 on this structure. However, to check the effect of the buckling amplitude on STM/STS, we also calculate the electronic structure for the c(4×2) structure experimentally proposed by Holland, Duke and Paton [108]. We will refer this structure
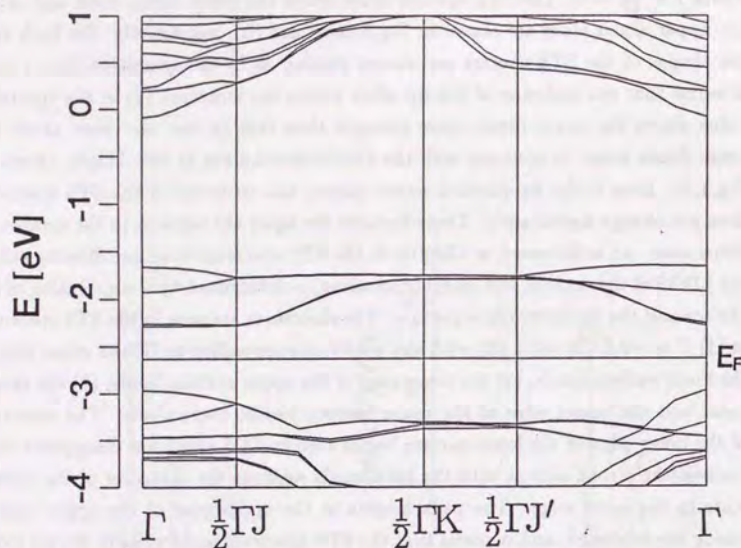
Figure 3.21: The calculated band dispersion relation of Si(001) c(4×2) surface, the HDP structure, is presented. The eight bands near the Fermi energy are surface bands.

as HDP structure. The structure is shown in Table 3.4 (b). In this structure, the buckling of the dimer is stronger and the upper dimer atom is farther from the second layer atoms, compared with the modified Yin-Cohen's structure. We use the two times larger rectangular surface unit cell, as before. One layer of hydrogens is also added to the opposite side of the slab, and the unit cell has the same number of atoms as that of modified Yin-Cohen's.

The calculated band dispersion relation is shown in the Fig.3.21. In the bulk band gap, there are also eight surface bands, but the lower four surface bands penetrate deeply in the bulk valence bands. This surface is also semiconducting, and the indirect surface band gap is 0.7eV, wider than that of modified Yin-Cohen's model (see Fig.3.15). The dispersions of surface bands are weaker, especially the lower four surface bands are very narrow localized bands. This comes from the strong buckling, and the lower surface states would be localized strongly on the upper dimer atom.
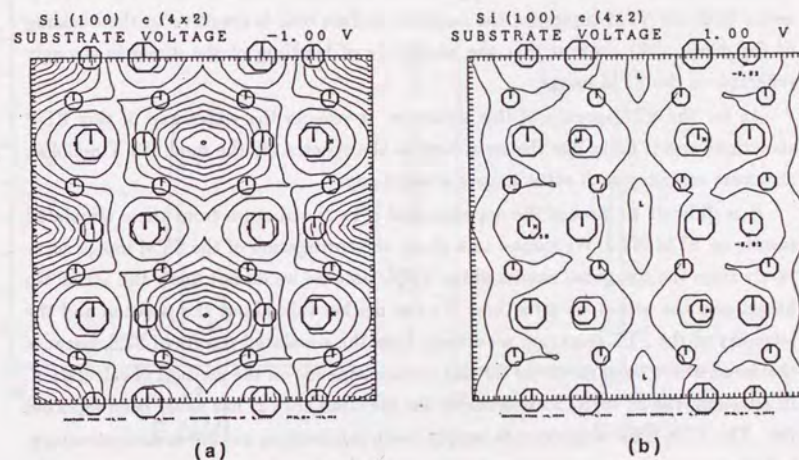
Figure 3.22: STM image of Si(001) c(4×2) HDP structure at the tip height, 10.0au (5.3Å), calculated by CVT method. (a) surface bias −1.0V [converted interval, 0.3Å] (b) +1.0V [converted interval, 0.3Å]

Calculated STM image of HDP structure is shown in Fig.3.22. The tip height is the same as in the case of modified Yin-Cohen's structure. The image of the negative surface bias does not change from that of modified Yin-Cohen's structure, except its corrugation is strongly enhanced to be about 3.0Å. For the positive surface bias case, its image and its corrugation does not change significantly. These are the result of the stronger localization of the wave function. The larger buckling leads to stronger splitting of the surface bands and the stronger localization of the wave functions of the surface bands either on the upper or on the lower dimer atoms. Therefore, it seems that the STM image for the negative surface bias is sensitive to the buckling of the dimer. We confirm that the amplitude of buckling of the dimer is strongly reflected on the STM image.

As for the STS spectra of this structure, it reflects the wider gap of this HDP structure, and it looks like the structures in the spectra for the modified Yin-Cohen structure repelling each other to give a wider gap.

It is difficult to discuss the experimental c(4×2) structure from these simulated results on STM/STS. We cannot talk about the corrugation of the STM image accurately from the simulated results of the STM, because we do not know the actual tip height and the actual tip structure. We can neither talk about the position and the intensity of the STS spectrum accurately from the simulated results of STS, because the detail of the band structure for this surface depends on the method of calculation. In addition, the STM/STS experiments for the clean c(4×2) has never been reported yet. The STM/STS experiments supply much information on the surface structure, but they only assist our understanding of the surface. We cannot determine the accurate atomic position only from the STM/STS experiments.

§5.   Comparison with the Ordinary LCAO Calculation

To examine the difference between the present CVT method and the ordinary LCAO method, we show the LDOS spectra at the tip height, 10au (5.3Å), calculated by CVT method and ordinary LCAO method in Fig.3.23 and Fig.3.24, respectively. The nodal feature of the upper surface band is reflected on the LDOS spectra for both cases, and all the presented spectra have a strong structure around the Fermi energy, but those spectra show some differences. In the ordinary LCAO method, the LDOS almost keeps the figure of the total DOS. This is the result of the decaying factor
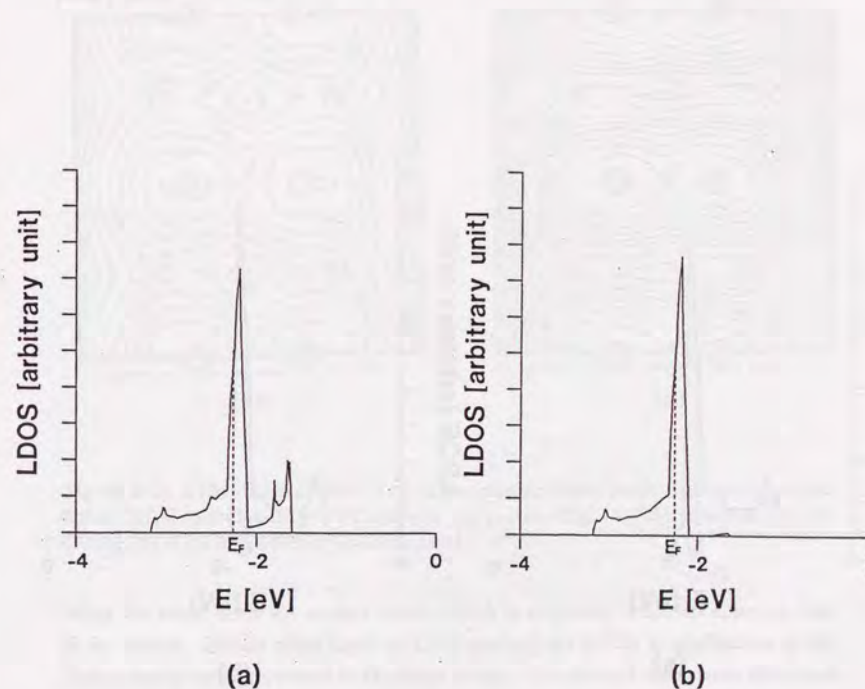
Figure 3.23: The LDOS spectrum of the Si(001) (2×1) symmetric dimer at the tip height, 10.0au (5.3Å), by calculated the CVT method, (a) above one of the dimer atom (b) above the middle of the dimer bridge.
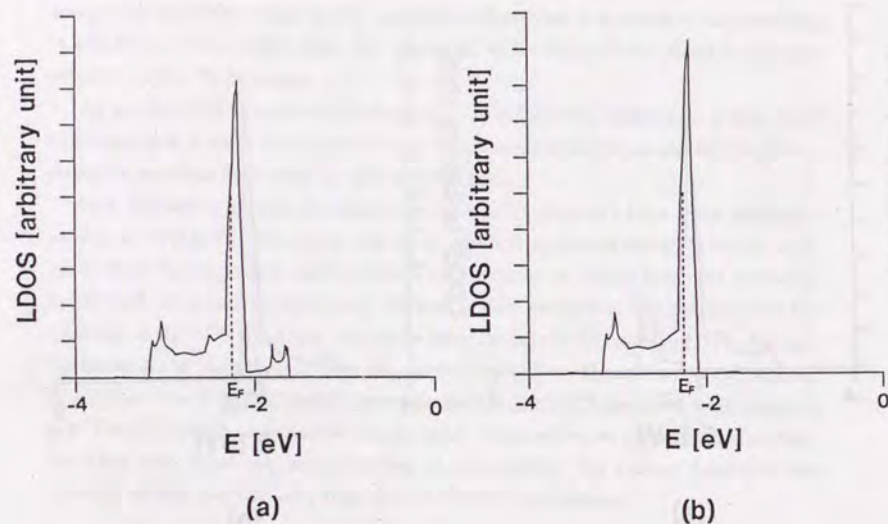
Figure 3.24: The LDOS spectrum of the Si(001) (2×1) symmetric dimer at the tip height, 10.0au (5.3Å), calculated straightforwardly from the LCAO wave functions. (a) above one of the dimer atom (b) above the middle of the dimer atom.
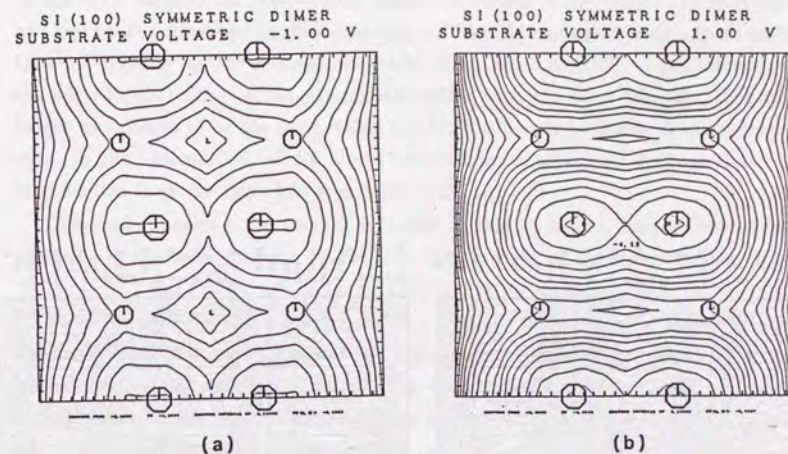
Figure 3.25: STM image of Si(001) (2×1) symmetric dimer surface at the tip height, 5.0au (2.7Å), calculated by CVT method. (a) surface bias −1.0V [converted interval, 0.06Å] (b) +1.0V [converted interval, 0.09Å]

being the same in all the surface bands, which is originated from the common base Si 2p orbital. On the other hand, in CVT method the LDOS is emphasized in the higher energy and suppressed in the lower energy. Our method reproduces the actual behavior of decay of the vacuum tail, but the ordinary LCAO method does not. In the calculation of the transfer matrix elements, the wave function of the lower surface state is convoluted with the wave function of the tip, which is more localized in the stronger region of the tip's potential. In our method, the different dependence of the decaying behavior on the energy is reduced by this mechanism, but in the ordinary LCAO method, this mechanism enhance the effect of the lower levels of the surface. Thus, the ordinary LCAO method overestimates the lower energy states and underestimates the higher energy states of the surface. These differences will affect the simulated results, in particular the absolute value of the tunneling current and the STS spectra.

Here we compare the results of the STM simulation by the two methods. Fig.3.25

S W10   D = 5.0 T = 0.0 P =
     Current   V =-1.00 DE =
Min= -3.94   Max= -1.67

S W10   D = 5.0 T = 0.0 P =
     Current   V = 1.00 DE =
Min= -3.80   Max=-0.998

(a)   (b)
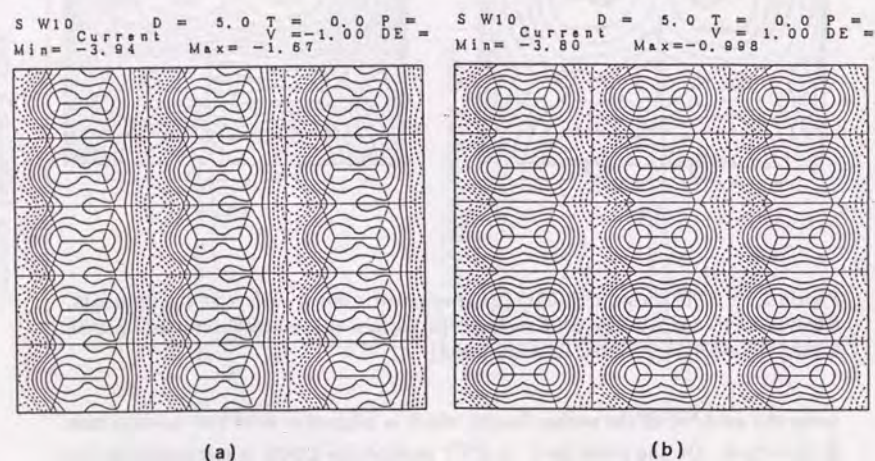
Figure 3.26: STM image of Si(001) (2×1) symmetric dimer surface at the tip height, 5.0au (2.7Å), calculated by the ordinary LCAO method. (a) surface bias −1.0V (b) +1.0V

shows the STM image of the symmetric dimer structure at the tip height 5.0au (2.7Å) by the CVT method. In both surface biases, the shapes of the images are bean-like and two peaks correspond to the dimer atoms. These figures could be compared with those of ordinary LCAO method by Isshiki *et al.*, Fig.3.26 [109]. They calculated the same Si(001) (2×1) symmetric dimer surface with the same W_{10} tip. The tip height was chosen to be the same, 5.0au (2.7Å). The figures look almost the same as ours. In their calculation, all tip atoms are considered, so the STM image shows a modification from the three-fold symmetry of the tip.

Rigorously speaking, our method is invalid at this tip height, because our representation of the wave function by the free wave is valid in the region farther than 10.0au (5.3Å) and not for this distance. But qualitative argument could be possible.

To summarize the above discussions, the ordinary LCAO method overestimates the lower levels and underestimates the higher ones because of its poor description of the decay of the wave function tail. This over/underestimating feature would be stronger when the tip position is farther from the surface. However, we cannot confirm any significant difference between the CVT method and the ordinary LCAO method from the comparison between Isshiki *et al.*'s calculation and ours. At least, when the tip height is about 5au, the ordinary LCAO method is as meaningful as our method.

§6.   Checking the Values of Parameters for the Connection of the Wave Functions

In this section, we check the validity of the choice of parameter values on the STM/STS simulation.

Firstly, we discuss the choice of the position of the intermediate-vacuum boundary. As mentioned before, the criteria are; (1) the 2D Fourier elements of the potential except for the $G_{\parallel} = (0, 0)$ element are negligibly small compared with the $G_{\parallel} = (0, 0)$ element, (2) the $G_{\parallel} = (0, 0)$ element is small enough compared with the work function, (3) the classical turning point for the Fermi level is enough inside the boundary so that the wave functions almost decay to zero near the boundary. Though the third rule depends on the choice of the model barrier, i.e. choice of position of the surface-intermediate boundary, all these criteria are reasonably satisfied at the point 10au (5.3Å) far from the outermost layer. At this point, in the case of the symmetric dimer surface, $G_{\parallel} = (1, 0)$ element of the potential is 0.04% of $G_{\parallel} = (0, 0)$ element, $G_{\parallel} = (0, 0)$ element is 14% of work function, and the position of the classical turning

point is less than 4.5au (2.4Å) from the outermost layer. We take this value for the calculations.

Next we discuss the choice of position of the surface-intermediate boundary. As mentioned before, this position has two meanings; (1) potential jumps up in order to reproduce the height of the potential barrier at this position, (2) the wave functions of the intermediate region and the surface region are connected at this position. (see Fig.2.1)

From the former point, the Si atomic radius, 1.32Å is a reference to determine the position. Since the potential barrier is a model in our method, the choice would have some ambiguity. It is possible to take into account the latter point by the choice of the cut-off, G_{c2}, in the reciprocal lattice vector expansion in the intermediate region. Thus, it is possible to choose the boundary to be 2au (1.1Å) far from the outermost layer.

As for the choice of the cut-off $|G_{c2}|$, it is reasonably chosen as 2.25Ry; the biggest but neglected element corresponding to $\mathbf{G}_\parallel = (5, 0)$ is 3% of $\mathbf{G}_\parallel = (0, 0)$ element at the position of 2au (1.1Å), and less at more distant point, in the case of the symmetric dimer surface.

We also check the jump of the derivative of the wave function at the surface-intermediate boundary in the calculation. The change of the eigenenergy of the wave function caused by the jump of the derivative can be estimated by δE defined in eq.(2.16). At the surface bands in the Si(001) (2×1) symmetric dimer case, $|\Psi_s(\mathbf{G}_\parallel, z = z_c)|$ is smaller than the order of 10^{-2}au, $|\frac{d}{dz}[\Psi_s - \Psi_m](\mathbf{G}_\parallel, z = z_c)|$ is smaller than the order of 10^{-3}au, and Ω_0 is the order of 10^2au. Then the value of δE is estimated as about 0.01eV. This value is small enough to neglect the change of the eigenenergy.

Finally, we studied the change in the STM image caused by the difference of the surface-intermediate boundary position. We calculate the STM images of the symmetric dimer surface in the cases of the boundary position of 1.5au (0.8Å) and 2.5au (1.3Å) from the outermost layer. The images are slightly different from that in the case of the boundary position, 1.0au, but do not change significantly.

The situation is similar for the case of the c(4×2) surface, but the cut-off $|G_{c2}|$ is reasonably chosen as 1.0Ry, because the number of the outermost layer's atom in unit area is one quarter of that of the symmetric dimer surface.

From these checks, it would be sure that the choices of the boundaries are reasonable enough and all the calculated results have enough validity within our model.

§7.   Non-buckled Image of STM Observation

Based on the above simulated results of STM/STS, we discuss the non-buckled dimer image observed in STM experiments. We can confirm that the non-buckled dimer image does not correspond to the symmetric dimer structure. The reasons are as follows.

According to the absolute value of the simulated tunneling current, the experimental tip height is 10Å from the outermost layer of the surface, and it would be even larger considering the effect of the image potential in the potential barrier. At this tip height, our simulation of the STM images of the symmetric dimer structure do not reproduce the experimental non-buckled images. If the tip height is smaller than 10Å, the simulated images show the bean-like image for both polarity, while the experimental non-buckled images show the nodal structure for the positive surface bias. In addition, the simulated STS spectrum does not reproduce the experimental one, either. Therefore, the experimental non-buckled images do not correspond to the symmetric dimer structure.

Let us discuss what the observed non-buckled image corresponds to. There were three possibilities as mentioned before. The first possibility is that the tip moves the surface atoms, but this should be rejected, because the tip-surface distance is larger than 10Å. But, if some insulating atoms are adsorbed on the tip, it would be possible that the tip position becomes smaller than 10Å. Anyhow it is difficult to recognize this possibility as the mechanism of non-buckled image.

The second possibility is that the asymmetric dimer can be seen as a non-buckled dimer, but this is also rejected. The corrugation of the STM image must reflect clearly the effect of the buckling of the dimer even in a large tip height.

The remaining possibility is that the dimers are actually buckling. This is supported by the fact that the experimental STS spectrum on the non-buckled image region seems to agree better with that calculated with the buckled c(4×2) structure. The buckling of the dimers oscillates thermally like a seesaw, and alter between the two structures, where one of the dimer atoms is upper or lower, in shorter time interval than the determination time of the tip height at each position in the STM observation. STM would observe the time average image of the oscillating buckled dimer. Then we could observe the oscillating asymmetric dimer as a symmetric dimer in STM. Thus it is interesting what we observe in the STM experiments of the Si(001) surface at low temperatures, where LEED experiments show clear c(4×2) pattern [76].

However, there remains a little possibility that the symmetric dimer structure

corresponds to the non-buckled STM image. If the probe orbitals of the tip have only s character around the z-axis and the tip height is about 10au, then the STM images may have similar corrugations to Fig.3.10 (b), (c) and Fig.3.11 (b), (c). If some insulating atoms are adsorbed on the tip top, there might be some possibility that both these conditions are satisfied and the non-buckled STM image can be obtained from the symmetric dimer structure.

Anyway, in order to confirm the original structure of the non-buckled dimer image of STM, it is necessary to simulate other dimer structures; (2×1) asymmetric dimer and $p(2 \times 2)$ structure, or buckled weakly, etc. It is also necessary to simulate the dimer structures with other kind of tips, such as a dirty tip adsorbing some insulating atoms.

Chapter 4

Concluding Remarks and Summary

§1.   Discussions on the Method

In our calculations presented in the previous sections, though we can well describe the exponential decay of the wave function tails, there remains some problems like the poor descriptions of the work function and the band gaps. These problems come solely from the usage of the LCAO-band method with isolated slab model. In order to avoid these problems, it would be better to use the plane wave band calculation with repeated slab model instead of the LCAO-band method. If we could apply our CVT method to the plane wave band calculation in some way, the simulation of STM/STS would be more realistic. This cannot be done in a parallel way with this work, but similar procedure may be worked out. It is very interesting to study this in the future.

We believe that our results are enough valuable and essential, but it would be necessary to do more accurate calculations so as to confirm validity of our results. However, such a calculation is difficult to carry out. Using LDA for the exchange-correlation potential estimates the band gaps of the energy bands smaller than the actual ones, while the localization of the wave functions partially cancels the effect of LDA in the LCAO-band method. In addition, we cannot identify the character of the tip actually, and it is difficult to reproduce the actual tunnel barrier potential.

With our method, we can treat the effect of the image potential or the electric field, if the tunnel barrier potential is given in some way or other. It is difficult to take these effects into account in the calculation with the ordinary LCAO method or the ordinary plane wave method without connecting the wave functions. It would be interesting to include the effect of the image potential or the electric field in STM/STS

simulation, even if the tunnel barrier is a model potential.

§2.   Summary

In this article, we develop a new theoretical method to simulate STM/STS. The method uses LCAO-band method with isolated slab model, but the wave functions are connected to 2D plane waves with damping factor outside the surface. Though there remain some problems of the LCAO-band method, the exponential decay of the wave functions of the surface are well described with this procedure. We apply this method to Si(001) reconstructed surfaces, and we find it difficult to obtain the experimental STM image of non-buckled (2×1) structure from (2×1) symmetric dimer structure. In addition, we confirm that the experimental $c(4 \times 2)$ image of STM is actually obtained from the $c(4 \times 2)$ structure and the buckling of the dimer is strongly reflected on the STM image.

The main results are as follows.

Comparing our CVT method with the ordinary LCAO method, we confirm that the lower surface ones are overestimated and the higher states are underestimated in the STM/STS simulation by the ordinary LCAO method. This over/underestimating feature is stronger when the tip position is farther from the surface. Comparing with our simulated STM results, the STM images of Isshiki *et al.*, calculated by the ordinary LCAO method, has enough validity at least in the case of the tip height, 5au.

Based on the calculated value of the tunneling current, the tip position is supposed to be about $10 \sim 12$Å from the surface, though this tip height would be an underestimation because our tunnel barrier model would be higher than the real potential barrier.

We cannot obtain the non-buckled dimer image of the STM observation from the symmetric dimer structure using the CVT method at the tip height 10au. This comes from our probe orbital character of the tip and the metallic character of the surface bands. Even if the tip moves higher, our calculated image remains different from the experimental one, because LDOS distribution map has peaks at the intermediate of the dimer bridges at that tip height. The calculated STS spectrum of symmetric dimer structure does not reproduce the experimental STS spectrum on the non-buckled image region.

In the case of $c(4 \times 2)$ structure, even if the tip height is about 10Å, the calculated STM images remind us of the structure of the surface and they have enough

corrugation. The calculated STS spectrum of this structure agrees well with the STS spectrum observed on the non-buckled dimer region.

We show that the splitting of the two bands is larger when the buckling of the dimer is stronger. This fact results in the stronger localization of the wave functions on the upper or lower dimer atom, and in the large corrugation for the negative surface bias image. In the negative surface bias image, not only the lower dimer atoms but also the upper dimer atoms are highlighted. The STM image certainly reflects the buckling of the dimer and the degree of the buckling. But the situation is not simple, and the real buckling amplitude is far smaller than the apparent corrugation of the image. Thus the zig-zag pattern observed in STM on Si(001) certainly corresponds to the buckling dimers, but the change of buckling amplitude would not be so strong as the apparent amplitude of the STM image.

Finally, according to our simulated results, we can discuss what STM observes in the non-buckled image region. Firstly, the tip position in the STM experiments would be larger than 10Å, so it is difficult for the tip to move one atom of the surface locally. Secondly, STM images reflect the buckling of the dimer strongly, so the STM image of buckling dimer does not correspond to the non-buckled image. Thirdly, it is reasonable to identify the experimental STS spectrum as that calculated for the $c(4 \times 2)$ structure. From these results, we conjecture that STM observes the buckled dimer which is oscillating quickly compared with the determination time of the tip height in the STM instrument.

Appendix A

Integration in Calculating Transfer Matrix Element

As shown in Chapter 3, we can calculate the transfer matrix as

$$M_{(\mathbf{k}_\parallel, n), \nu}(\mathbf{R}) = \sum_{\mathbf{G}_\parallel} D(\mathbf{k}_\parallel, n; \mathbf{G}_\parallel) \sum_a \sum_{\alpha \in a} C_\alpha^\nu \sum_i A_{\alpha, i}^a \sum_{a', i'} A_{V, i'}^{a'} J(\mathbf{k}_\parallel, n, \mathbf{G}_\parallel, \nu, a, \alpha, i, a', i'),$$

(A.1)

where

$$\begin{aligned}
J(\mathbf{k}_\parallel, n, \mathbf{G}_\parallel, \nu, a, \alpha, i, a', i') &= \int d^2 \mathbf{r}_\parallel e^{i(\mathbf{k}_\parallel + \mathbf{G}_\parallel) \cdot \mathbf{r}_\parallel - \kappa(E(\mathbf{k}_\parallel, n), \mathbf{k}_\parallel + \mathbf{G}_\parallel)z} \\
&\quad \times \mathcal{Y}_{lm} \overline{(\mathbf{r} - \mathbf{R}_a - \mathbf{R})} \, |\mathbf{r} - \mathbf{R}_a - \mathbf{R}|^l \\
&\quad \times e^{-B_{\alpha, i}^a (\mathbf{r} - \mathbf{R}_a - \mathbf{R})^2} \frac{e^{-B_{V, i'}^{a'} (\mathbf{r} - \mathbf{R}_{a'} - \mathbf{R})^2}}{|\mathbf{r} - \mathbf{R}_{a'} - \mathbf{R}|}.
\end{aligned}$$

(A.2)

$\mathcal{Y}_{lm}$ is the real type of spherical harmonic function. Here we show how to estimate the integral in eq.(A.2). We can rewrite $J(\mathbf{k}_\parallel, n, \mathbf{G}_\parallel, \nu, a, \alpha, i, a', i')$ as

$$J(\mathbf{k}_\parallel, n, \mathbf{G}_\parallel, \nu, a, \alpha, i, a', i') = e^{i(\mathbf{k}_\parallel + \mathbf{G}_\parallel) \cdot (\mathbf{R}_{a', \parallel} + \mathbf{R}_\parallel) - \kappa(E(\mathbf{k}_\parallel, n), \mathbf{k}_\parallel + \mathbf{G}_\parallel)(Z_{a'} + Z)} U_{lm}. \quad (A.3)$$

We must estimate the following type of integral, U_{lm}.

$$U_{lm} = \int d^2 \mathbf{r}_\parallel e^{i\mathbf{k} \cdot \mathbf{r} - \tau \cdot \mathbf{r}} \mathcal{Y}_{lm} \overline{(\mathbf{r} - \mathbf{r}_c)} \, |\mathbf{r} - \mathbf{r}_c|^l e^{-\beta_1 (\mathbf{r} - \mathbf{r}_c)^2} \frac{e^{-\beta_2 r^2}}{r}. \quad (A.4)$$

Notice that U_{lm} does not depend on the tip position, $\mathbf{R}$. We need to estimate these integral for $l = 0, 1, 2$.

[A] $l = 0$ **Case**

77

In the $l = 0$ case, U_s is estimated as

$$
\begin{aligned}
U_s &= \sqrt{\frac{1}{4\pi}} \int d^3\mathbf{r} \frac{1}{r} \exp\left[i\mathbf{k}\cdot\mathbf{r} - (\beta_1+\beta_2)\left|\mathbf{r} - \frac{\beta_1}{\beta_1+\beta_2}\mathbf{r}_c\right| - \frac{\beta_1\beta_2}{\beta_1+\beta_2}r_c^2 - \tau\cdot\mathbf{r}\right], \\
&= \sqrt{\frac{1}{4\pi}}\frac{2\pi}{\beta\lambda}\left[\int_0^\lambda e^{-X^2}dX\right]e^{-\beta_1 r_c^2 + \lambda^2},
\end{aligned}
\tag{A.5}
$$

where

$$
\lambda = \frac{\sqrt{(\beta_1\mathbf{r}_c - \frac{1}{2}\tau + \frac{i}{2}\mathbf{k})^2}}{\sqrt{\beta_1+\beta_2}}.
\tag{A.6}
$$

[B] $l = 1$ Case

In the $l = 1$ case, U_{p_x} can be estimated from U_s as

$$
\begin{aligned}
U_{p_x} &= \sqrt{3}\frac{1}{2\beta_1}\frac{\partial}{\partial x_c}U_s \\
&= \sqrt{3}\Lambda_x\left(-\frac{1}{\lambda}U_s + \frac{1}{\lambda}Q + 2\lambda U_s\right) + \sqrt{3}X_c U_s,
\end{aligned}
\tag{A.7}
$$

where

$$
\Lambda_x = \frac{1}{2(\beta_1+\beta_2)}\left(\beta_1 x_c - \frac{1}{2}\tau_x + \frac{i}{2}k_x\right)\frac{1}{\lambda},
\tag{A.8}
$$

$$
X_c = -x_c,
\tag{A.9}
$$

$$
Q = \sqrt{\frac{1}{4\pi}}\frac{2\pi}{\beta}e^{-\beta_1 r_c^2}.
\tag{A.10}
$$

U_{p_y} and U_{p_z} are estimated in the same way.

[C] $l = 2$ Case

In the $l = 2$ case, $U_{d_{xy}}$ is estimated from U_{p_x} as

$$
\begin{aligned}
U_{d_{xy}} &= \sqrt{5}\frac{1}{2\beta_1}\frac{\partial}{\partial y_c}U_{p_x} \\
&= \sqrt{15}\Lambda_x\Lambda_y\left[\left(\frac{3}{\lambda^2} - 4 + 4\lambda^2\right)U_s + \left(2\sqrt{\frac{1}{4\pi}} - \frac{3}{\lambda^2}Q\right)\right] \\
&\quad + \sqrt{15}(X_c\Lambda_y + Y_c\Lambda_x)\left(-\frac{1}{\lambda}U_s + \frac{1}{\lambda}Q + 2\lambda U_s\right) \\
&\quad + \sqrt{15}X_c Y_c U_s.
\end{aligned}
\tag{A.11}
$$

$U_{d_{yz}}$ and $U_{d_{zx}}$ are estimated in the same way. $U_{d_{x^2-y^2}}$ is estimated from U_{p_x} and U_{p_y} as

$$
U_{d_{x^2-y^2}} = \sqrt{\frac{15}{4}}\frac{1}{2\beta_1}\frac{\partial}{\partial x_c}U_{p_x} - \sqrt{\frac{15}{4}}\frac{1}{2\beta_1}\frac{\partial}{\partial y_c}U_{p_y}
$$

$$
\begin{aligned}
&= \sqrt{\frac{15}{4}}(\Lambda_x^2 - \Lambda_y^2)\left[\left(\frac{3}{\lambda^2} - 4 + 4\lambda^2\right)U_s + \left(2\sqrt{\frac{1}{4\pi}} - \frac{3}{\lambda^2}Q\right)\right] \\
&\quad + \sqrt{\frac{15}{4}}2(X_c\Lambda_x + Y_c\Lambda_y)\left(-\frac{1}{\lambda}U_s + \frac{1}{\lambda}Q + 2\lambda U_s\right) \\
&\quad + \sqrt{\frac{15}{4}}(X_c^2 - Y_c^2)U_s.
\end{aligned}
\tag{A.12}
$$

$U_{d_{z^2}}$ is estimated in the same way.

Thus, all U_{lm} can be calculated, if only U_s is calculated. U_s has only 1D integral, whose integrand is smooth and decays rapidly. Therefore we can easily evaluate all these integrals numerically.

References

[1] G. Binnig, H. Rohrer, Ch. Gerber, and E. Weibel, Phys. Rev. Lett. **49**, 57 (1982).

[2] G. Binnig and H. Rohrer, Review of Modern Phys. **59**, 615 (1987).
P. Hansma and J. Tersoff, J. Appl. Phys. **61**, R1 (1987).
R. V. Coleman, B. Giambattista, P. K. Hansma, A. Johnson, W. W. McNairy, and C. G. Slough, Advances in Phys. **37**, 559 (1988).
C. F. Quate, Phys. Today **August**, 26 (1986).

[3] G. Binnig, H. Fuchs, Ch. Gerber, H. Rohrer, E. Stoll, and E. Tosatti, Europhys. Lett. **1**, 31 (1986).

[4] S. Park and C. F. Quate, Appl. Phys. Lett. **48**, 112 (1986).

[5] I. P. Batra, N. Garcia, H. Rohrer, H. Salemink, E. Stoll, and S. Ciraci, Surf. Sci. **181**, 126 (1987).

[6] D. Tomanek, S. Louie, H. J. Mamin, D. W. Abraham, R. E. Thomson, E. Ganz, and J. Clarke, Phys. Rev. **B35**, 7790 (1987).

[7] D. Tomanek and S. G. Louie, Phys. Rev. **B37**, 8327 (1988).

[8] G. Binnig, H. Rohrer, Ch. Gerber, and E. Weibel, Phys. Rev. Lett. **50**, 120 (1983).

[9] K.Takayanagi, Y. Tanishiro, M. Takahashi, and S. Takahashi, J. Vac. Sci. Technol. **A3**, 1502 (1985), and references therein.

[10] R. M. Tromp, R. J. Hamers, and J. E. Demuth, Phys. Rev. **B34**, 1388 (1986).

[11] R. S. Becker, J. A. Golovchenko, E. G. McRae, and B. S. Swartzentruger, Phys. Rev. Lett. **55**, 2028 (1985).

[12] R. J. Hamers, R. M. Tromp, and J. E. Demuth, Phys. Rev. Lett. **56**, 1972 (1986)

[13] R. J. Hamers, R. M. Tromp, and J. E. Demuth, Surf. Sci. **181**, 346 (1987).

[14] G. Binnig and H. Rohrer, Surf. Sci. **126**, 236 (1983).

[15] G. Binnig, H. Rohrer, Ch. Gerber, and E. Weibel, Surf. Sci. **131**, L379 (1983)

[16] G. Binnig, H. Rohrer, Ch. Gerver, and E. Stoll, Surf. Sci. **144**, 321 (1984).

[17] R. J. Behm, W. Hösler, E. Ritter, and G. Binnig, Phys. Rev. Lett. **55**, 951 (1985).

[18] L. Vazquez, J. M. Rodrigurez, J. G. Herrero, A. M. Baro, N. Garcia, J. C. Canullo, and A. J. Arvia, Surf. Sci. **181**, 98 (1987).

[19] J. K. Gimzewski, A. Humbert, J. G. Bednorz, and B. Reihl, Phys. Rev. Lett. **55**, 951 (1985).

[20] J. K. Gimzewski, A. Humbert, J. G. Bednorz, and B. Reihl, Phys. Rev. **B33**, 690 (1986).

[21] V. M. Hallmark, S. Chiang, J. F. Rabolt, J. D. Swalen, and R. J. Wilson, Phys. Rev. Lett. **59**, 2879 (1987).

[22] J. Wintterlin, J. Wiechers, H. Brune, and T. Gritch, Phys. Rev. Lett. **62**, 59 (1989).

[23] J. K. Gimzewski, E. Stoll, and R. R. Schlittler, Surf. Sci. **181**, 267 (1987).

[24] P. H. Lippel, R. J. Wilson, M. D. Miller, Ch. Wöll, and S. Chiang, Phys. Rev. Lett. **62**, 171 (1989).

[25] H. Ohtani, R. J. Wilson, S. Chiang, and C. M. Mate, Phys. Rev. Lett. **60**, 2398 (1988).

[26] G. Binnig and H. Rohrer, Trends Phys. **1984**, 38.

[27] A. M. Baro, R. Miranda, J. Alanan, N. Garcia, G. Binnig, H. Rohrer, Ch. Gerber, and J. L. Carrascosa, Nature **315**, 253 (1985).

[28] D. L. Dorset, A. Engel, M. Häner, A. Massalski, and J. P. Rosenbusch, J. Mol. Biol. **165**, 701 (1985).

[29] R. M. Feensta, J. A. Stroscio, and A. P. Fein, Surf. Sci. **12** 95 (1987).

[30] Ph. Avouris and R. Wolkow, Phys. Rev. **39**, 5091 (1989).

[31] G. Binnig, C. F. Quate, and C. G. Gerber, Phys. Rev. Lett. **56**, 930 (1986).

[32] D. M. Eigler and E. K. Schweizer, Nature **344**, 524 (1990).

[33] R. Wilkins, E. Ben-Jacob, and R. C. Jaklevic, Phys. Rev. Lett. **63**, 801 (1989).

[34] P. Bedrossian, R. D. Meade, K. Mortensen, D. M. Chen, J. A. Golovchenko, and D. Vanderbilt, Phys. Rev. Lett. **63**, 1257 (1989).

[35] M. Tsukada, K. Kobayashi and S. Ohnishi, J. Vac. Sci. Tech. A8, 160 (1990).

[36] J. G. Simmons, J. Appl. Phys. **34**, 1793 (1963).

[37] C. B. Duke, "Tunneling in Solid", in *Solid State Physics*, ed. by F. Seitz, D. Turnbull and H. Ehrenreich, Academic Press (1969).

[38] N. M. Miskovsky, P. H. Cutler, and T. E. Feuchtwang, Appl. Phys. A27, 139 (1982).

[39] H. Q. Nguyen, P. H. Cutler, T. E. Feuchtwang, N. Miskovsky, and A. A. Lucas, Surf. Sci. **146**, 405 (1984).

[40] H. Q. Nguyen, P. H. Cutler, T. E. Feuchtwang, N. Miskovsky, and A. A. Lucas, Surf. Sci. **160**, 331 (1985).

[41] J. Bono and R. H. Good Jr., Surf. Sci. **151**, 543 (1985).

[42] B. Das and J. Mahanty, Phys. Rev. Lett. **36**, 898 (1987).

[43] N. Garcia, C. Ocal and F. Flores, Phys. Rev. Lett. **50**, 2002 (1983).

[44] E. Stoll, A. Baratoff, A. Selloni, and P. Carnevali, J. Phys. C17, 3073 (1984).

[45] G. Binnig, N. Garcia, H. Rohrer, J. M. Soler, and F. Flores, Phys. Rev. **B30**, 4816 (1984).

[46] L. Orosz and E. Balazs, Surf. Sci. **177**, 444 (1986).

[47] H. Morawitz, I. P. Batra, R. Reinisch, and G. R. Henry, Surf. Sci. **180**, 333 (1987).

[48] A. A. Lucas, H. Morawitz, G. R. Henry, J. P. Vigheron, Ph. Lambin, P. H. Cutler, and T. E. Feuchtwang, Phys. Rev. **B37**, 10708 (1988).

[49] J. Bardeen, Phys. Rev. Lett. **15**, 57 (1961).

[50] J. Tersoff and D. R. Hamann, Phys. Rev. Lett. **50**, 1998 (1983).

[51] J. Tersoff and D. R. Hamann, Phys. Rev. **B31**, 805 (1985).

[52] R. V. Coleman, B. Drake, P. K. Hansma, and G. Slough, Phys. Rev. Lett. **55**, 394 (1985).

[53] J. Tersoff, Phys. Rev. Lett. **57**, 440 (1986).

[54] J. Tersoff, Phys. Rev. **B39**, 1052 (1989).

[55] N. D. Lang, Phys. Rev. Lett. **55**, 230 (1985).

[56] N. D. Lang, Phys. Rev. Lett. **56**, 1164 (1986).

[57] N. D. Lang, Phys. Rev. Lett. **58**, 45 (1987).

[58] N. D. Lang, Phys. Rev. **B34**, 5947 (1986).

[59] N. D. Lang, Phys. Rev. **B36**, 8173 (1987).

[60] C. J. Chen, J. Vac. Sci. Tech. **A6**, 319 (1988).

[61] M. Tsukada and N. Shima, J. Phys. Soc. Japan **56**, 2875 (1987).

[62] N. Isshiki, K. Kobayashi, and M. Tsukada, Surf. Sci. **238**, L439 (1990); J. Vac. Sci. Tech. *in press.*

[63] K. Kobayashi and M. Tsukada, Solid State Comm. **74**, 1187 (1990).

[64] K. Kobayashi and M. Tsukada, Surf. Sci. *to be published.*

[65] A. Selloni, P. Carnevali, E. Tosatti, and C. D. Chen, Phys. Rev. **B31**, 2602 (1985).

[66] R. E. Schlier and H. E. Farnsworth, J. Chem. Phys. **30**, 917 (1959).

[67] F. Jona, H. D. Shih, A. Ignatiev, D. W. Jepsen, and P. M. Marcus, J. Phys. **C10**, L67 (1977).

[68] S. J. White and D. P. Woodcuff, Surf. Sci. **64**, 131 (1977).

[69] S. Y. Tong and A. L. Maldondo, Surf. Sci. **78**, 459 (1978).

[70] M. J. Cardillo and G. E. Becher, Phys. Rev. **B21**, 1497 (1980).

[71] J. Ihm, D. H. Lee, J. D. Jannopoulos, and J. J. Xiong, Phys. Rev. Lett. **51**, 1872 (1983).

[72] J. J. Lander and J. Morrison, J. Chem. Phys. **37**, 729 (1962).

[73] T. D. Poppendieck, T. C. Ngoc, and M. B. Webb, Surf. Sci. **43**, 647 (1974).

[74] T. D. Poppendieck, T. C. Ngoc, and M. B. Webb, Surf. Sci. **75**, 287 (1978).

[75] M. Aono, Y. Hou, C. Oshima, and Y. Ishizawa, Phys. Rev. Lett. **49**, 567 (1982).

[76] T. Tabata, T. Aruga, and Y. Murata, Surf. Sci. **179**, L63 (1986).

[77] H. Wang, R. Lin, and X. Wang, Phys. Rev. **B36**, 7712 (1987).

[78] J. A. Martin, D. E. Savage, W. Moritz, and M. G. Lagally, Phys. Rev. Lett. **56**, 1936 (1986).

[79] T. Aruga and Y. Murata, Phys. Rev. **B34**, 5654 (1986).

[80] J. A. Appelbaum and D. R. Hamann, Surf. Sci. **74**, 21 (1978).

[81] D. J. Chadi, Phys. Rev. Lett. **43**, 43 (1979).

[82] J. Ihm, M. L. Cohen, and D. J. Chadi, Phys. Rev. **B21**, 4592 (1980).

[83] M. T. Yin and M. L. Cohen, Phys. Rev. **B24**, 2303 (1981).

[84] G. P. Kerker, S. G. Louie, and M. L. Cohen, Phys. Rev. **B17**, 706 (1978).

[85] W. S. Verwoerd, Surf. Sci. **103**, 404 (1981).

[86] W. S. Yang, F. Jona, and P. M. Marcus, Phys. Rev. **B28**, 2049 (1983).

[87] R. M. Tromp, R. J. Hamers, and J. E. Demuth, Phys. Rev. Lett. **55**, 1303 (1985).

[88] R. J. Hamers, R. M. Tromp, and J. E. Demuth, Phys. Rev. **B34**, 5343 (1986).

[89] R. Seiwatz, Surf. Sci. **2**, 473 (1964).

[90] D. J. Chadi, J. Vac. Sci. Tech. **16**, 1290 (1979).

[91] J. E. Northrup, Phys. Rev. Lett. **54**, 815 (1985).

[92] J. C. Phillips, Surf. Sci. **40**, 459 (1973).

[93] Z. Zhu, N. Shima, and M. Tsukada, Phys. Rev. **B40**, 11868 (1989).

[94] F. J. Himpsel and D. E. eastman, J. Vac. Sci. Tech. **16**, 1297 (1979).

[95] R. I. G. Uhrberg, G. V. Hansson, J. M. Nicholls, and S. A. Flodstrom, Phys. Rev. **B24**, 4684 (1981).

[96] J. E. Rowe and H. Ibach, Phys. Rev. Lett. **32**, 421 (1974).

[97] H. A. Van Hoof and M. J. Van der Wiel, Appl. Surf. Sci. **6**, 444 (1980).

[98] S. Kono, Phys. Rev. B, *in press.*

[99] R. J. Hamers, Ph. Avouris, and F. Bozso, Phys. Rev. Lett. **59**, 2071 (1987).

[100] S. Ohnishi and M. Tsukada, Solid State Comm. **71**, 391 (1989).

[101] J. Tersoff, Phys. Rev. **B40**, 11990 (1989).

[102] N. Shima, J. Phys. Soc. Japan **52**, 578 (1983).

[103] A. Zunger and A. J. Freeman, Phys. Rev. **B15**, 4716 (1977).

[104] N. D. Lang, in *Solid States Physics*, **28**, 225, ed. by H. Ehrenzeich, F. Seitz, and D. Turnbull, Academic Press (1973).

[105] D. E. Ellis and G. S. Painter, Phys. Rev. **B2**, 2887 (1970).

[106] L. F. Mattheiss, Phys. Rev. **139**, A1893 (1965).

[107] J. D. Levine, Surf. Sci. **34**, 90 (1973).

[108] B. W. Holland, C. B. Duke and A. Paton, Surf. Sci. **140**, L269 (1984).

[109] N. Isshiki, private communication.